ENVIRONMENTAL RESEARCH
CLIMATE

OPEN ACCESS

RECEIVED
10 December 2025

REVISED
23 February 2026

ACCEPTED FOR PUBLICATION
18 March 2026

PUBLISHED
7 April 2026

PAPER

Decomposing the global and regional aerosol effective radiative forcing associated with strong versus weak air quality policies by Mid-21st century

Robert J Allen[1,*], Laura J Wilcox[2], Bjørn H Samset[3], Sharar Ahmadi[2], Annica M L Ekman[4], Maxwell T Elling[5,6], Luke Fraser-Leach[7], Paul Griffiths[8], James Keeble[9], Tsuyoshi Koshiro[10], Paul Kushner[7], Anna Lewinschal[4], Molly MacRae[11,12], Risto Makkonen[13], Joonas Merikanto[13], Pierre Nabat[14], Larissa Nazarenko[15,16], Declan O'Donnell[13], Naga Oshima[10], David Paynter[17], Geeta Persad[18], Steven T Rumbold[2], Neil Swart[19], Toshihiko Takemura[20], Kostas Tsigaridis[15,16], Knut von Salzen[19,21] and Daniel M Westervelt[16,22]

[1] Department of Earth and Planetary Sciences, University of California, Riverside, CA, United States of America
[2] National Centre for Atmospheric Science, University of Reading, Reading, United Kingdom
[3] CICERO Center for International Climate Research, Oslo, Norway
[4] Department of Meteorology, Stockholm University, Bolin Centre for Climate Research, Stockholm, Sweden
[5] Department of Atmospheric and Oceanic Sciences, University of Colorado Boulder, Boulder, CO, United States of America
[6] Cooperative Institute for Research in Environmental Sciences, University of Colorado Boulder, Boulder, CO, United States of America
[7] Department of Physics, University of Toronto, Toronto, Canada
[8] School of Chemistry, University of Bristol, Bristol, United Kingdom
[9] Lancaster Environment Centre, Lancaster University, Lancaster, United Kingdom
[10] Meteorological Research Institute, Japan Meteorological Agency, Ibaraki, Japan
[11] Rutherford Appleton Laboratory, Centre for Environmental Data Analysis, Science & Technology Facilities Council, Didcot, United Kingdom
[12] Department of Meteorology, University of Reading, Reading, United Kingdom
[13] Finnish Meteorological Institute, Helsinki, Finland
[14] Météo-France, CNRS, University Toulouse, CNRM, Toulouse, France
[15] Center for Climate Systems Research, Columbia University, Palisades, NY, United States of America
[16] NASA Goddard Institute of Space Studies, New York, NY, United States of America
[17] NOAA/Geophysical Fluid Dynamics Laboratory, Princeton, NJ, United States of America
[18] Department of Geological Sciences, The University of Texas at Austin, Austin, TX, United States of America
[19] Canadian Centre for Climate Modelling and Analysis, Environment and Climate Change Canada, Victoria, BC, Canada
[20] Research Institute for Applied Mechanics, Kyushu University, Fukuoka, Japan
[21] Department of Atmospheric and Climate Science, University of Washington, Seattle, WA, United States of America
[22] Lamont-Doherty Earth Observatory, Columbia Climate School, New York, NY, United States of America
[*] Author to whom any correspondence should be addressed.

E-mail: rjallen@ucr.edu

Keywords: aerosols, effective radiative forcing, aerosol-cloud interactions, aerosol-radiation interactions, Regional Aerosol Model Intercomparison Project

Supplementary material for this article is available online

Abstract

The Regional Aerosol Model Intercomparison Project (RAMIP) is designed to quantify the forcing and climate impacts of mid-21st century anthropogenic aerosol and precursor gas (AA) emissions reductions (both industrial and biomass burning), by comparing a weak (SSP3-7.0) versus strong (SSP1-2.6) level of air quality control aerosol emissions pathway. AA emissions reductions experiments include global (GLO), East Asia (EAS), South Asia, Africa and the Middle East (AFR), and North America and Europe (NAE). Here, we use RAMIP time-slice simulations with fixed sea surface temperatures and sea-ice distributions from nine models to quantify the aerosol effective radiative forcing (ERF), including aerosol radiation (ERF_{ari}) and aerosol cloud interactions (ERF_{aci}). The multi-model global mean net $ERF_{ari+aci}$ is 0.77 ± 0.25 W m^{-2} for GLO, and three of the four regional perturbations yield a significant positive net $ERF_{ari+aci}$ (up to 0.15 ± 0.07 W m^{-2} for EAS). In all cases, net $ERF_{ari+aci}$ is dominated by aerosol-cloud interactions, which are largely due to reduced cloud scattering. Of the four regions, NAE yields the largest forcing efficiency

whereas AFR yields the weakest. Although the areas outside our four target regions contribute 25% to the GLO aerosol optical depth reduction, they disproportionately contribute 44% to the GLO net $ERF_{ari+aci}$. The multimodel regional mean net $ERF_{ari+aci}$ for three regional perturbations is much larger (up to 1.64 ± 1.36 W m^{-2} for EAS) than the corresponding global mean value. However, these regional values are even larger (up to 2.69 ± 1.72 W m^{-2} for EAS) under global aerosol reductions, implying remote emission reductions represent a sizable contribution (up to 1.05 ± 0.56 W m^{-2} for EAS). These large regional ERFs will in turn drive relatively large regional climate impacts, which continue to be underappreciated in most policy discussions.

1. Introduction

Anthropogenic aerosols (AAs) are small (nano-micrometer-sized) suspended particles, emitted directly from human activities or formed in the atmosphere from precursor gases (Myhre *et al* 2013, Szopa *et al* 2021). Unlike long-lived greenhouse gases (GHGs), AAs are short-lived with atmospheric lifetimes of days to weeks, and are concentrated near their sources (Boucher *et al* 2013). AAs modify Earth's top-of-the-atmosphere (TOA) energy balance through radiative and cloud microphysical pathways, commonly referred to as aerosol-radiation interactions and aerosol-cloud interactions, respectively (Bellouin *et al* 2020). Aerosol-radiation interactions include the direct scattering and absorption of radiation. Sulfate, nitrate, ammonium, and many organic aerosols are predominantly scattering and exert a cooling influence. Black carbon (BC) is the primary absorbing aerosol, which warms the atmosphere, dims the surface, stabilizes the boundary layer, and can reduce low-cloud cover (the 'semi-direct' effect), which acts to offset the cooling from scattering aerosol species (Koch and Del Genio 2010, Allen *et al* 2010, Stjern *et al* 2017, Allen *et al* 2019). Aerosol-cloud interactions include indirect effects on clouds (Boucher *et al* 2013, Gryspeerdt *et al* 2017, Bellouin *et al* 2020, Quaas *et al* 2020, Rosenfeld *et al* 2023). The first indirect effect, also referred to as the cloud albedo effect or Twomey effect, refers to increased aerosol concentrations leading to more cloud condensation nuclei (CCN), increasing cloud droplet concentration and cloud optical thickness, with a subsequent reduction in droplet size and an increase in cloud albedo (Twomey 1974, 1977). The second indirect effect, more commonly known as the cloud lifetime effect or Albrecht effect, associates increases in aerosol to a reduction in cloud droplet size, which affects precipitation efficiency with a tendency to increase liquid water content, cloud lifetime (Albrecht 1989), and cloud thickness (Pincus and Baker 1994). Of the above mentioned aerosol species, sulfate is a very efficient CCN as it is highly soluble in water.

The aerosol effective radiative forcing (ERF) aggregates the direct scattering and absorption of radiation (ERF_{ari}) with the indirect effects on clouds (ERF_{aci}). As reported in the IPCC Sixth Assessment Report (AR6), the total ERF due to aerosols is estimated at -1.3 (-2.0 to -0.6) W m^{-2} from 1750–2014 (Forster *et al* 2021). This is largely dominated by ERF_{aci} at -1.0 (-1.7 to -0.3) W m^{-2}, which is largely associated with anthropogenic emissions of sulfur dioxide (SO_2) and subsequent oxidation to sulfate aerosol (Thornhill *et al* 2021, Kalisoras *et al* 2024). ERF_{ari} is estimated to be about 30% of ERF_{aci} at -0.3 (-0.6–0.0) W m^{-2} (Forster *et al* 2021). Similar values are obtained in several other studies (Bellouin *et al* 2020, Smith *et al* 2020, Zelinka *et al* 2023, Kalisoras *et al* 2024). Thus, the historical AA buildup has acted to mute GHG warming, with an estimated global mean annual mean cooling of around 0.5 (0.22 °C–0.96) °C (Forster *et al* 2021, Masson-Delmotte *et al* 2021).

The relatively large spread in aerosol ERF remains the largest source of uncertainty in future climate change projections (Forster *et al* 2021, Watson-Parris and Smith 2022). This uncertainty stems from a multitude of factors including the complex interactions between aerosols, radiation and clouds, uncertain emission inventories, limited observational constraints, coarse grid resolution, and uncertain parameterizations of aerosol processes (e.g. transport, removal, chemistry, optical properties, hygroscopicity, aging, mixing state, ability to act a CCN). In particular, the major sources of uncertainty in climate models' representation of aerosol-cloud interactions include aerosol interactions with mixed-phase, convective, and ice clouds; contributions from aerosols to act as ice nucleating particles; and aerosol-induced adjustments in cloud liquid water path and cloud cover (Forster *et al* 2021).

Efforts to improve air quality have led to aerosol emission reductions, beginning in the US and Europe in the late 1970s/early 1980s, and more recently in China in the early 2000s (e.g. Hoesly *et al* 2018, Zhang *et al* 2018, Aas *et al* 2019, Samset *et al* 2019, McDuffie *et al* 2020). The collapse of the Soviet Union also led to reduced aerosol pollution in the late 1980s/early 1990s. More recent efforts to clean up shipping emissions (e.g. SO_2, a precursor to sulfate aerosol) have also contributed (Diamond 2023, Gettelman *et al* 2024, Jordan and Henry 2024, Quaglia and Visioni 2024, Skeie *et al* 2024, Yoshioka *et al*

2024, Yuan *et al* 2024, Benas *et al* 2025, Watson-Parris *et al* 2025). These endeavors have led to a recent (∼2000) reversal in the aerosol ERF trend (Quaas *et al* 2022, Hodnebrog *et al* 2024), further strengthening Earth's positive energy imbalance and likely leading to enhanced warming (Samset *et al* 2025). Such aerosol emission reductions are expected to continue into the future, with some emissions trajectories yielding aerosol reductions by mid-21st century as large in magnitude as the historical buildup (Persad *et al* 2023). This has led to more concerted efforts to understand the climate implications of future aerosol emission reductions, including the impacts of regional aerosol emission changes (Westervelt *et al* 2015, Acosta-Navarro *et al* 2017, Westervelt *et al* 2017, Myhre *et al* 2017, Allen *et al* 2020, Wilcox *et al* 2020, Liu *et al* 2018, Persad *et al* 2023, Samset *et al* 2024, von Salzen *et al* 2025, Griffiths *et al* 2025). Their influences are distinct and markedly more uncertain and spatially heterogeneous as compared to continued increases in well-mixed, long-lived GHGs. This applies to the ERF induced by aerosol emission changes, their influence on global mean surface temperature and precipitation, and in particular, their influence on the regional and seasonal pattern of impact-relevant climate hazards (e.g. Allen *et al* 2024, Iles *et al* 2024).

The Regional Aerosol Model Intercomparison Project (RAMIP) contains a comprehensive suite of simulations from CMIP6-era global climate models, specifically designed to improve our understanding of these issues (Wilcox *et al* 2023). The focus on transient regional aerosol emission reductions is intended to provide a more direct link to policy decisions than global emission perturbations, while also allowing for improved understanding of aerosol transport, air quality, regionally specific climate interactions, as well as teleconnections and remote impacts. Here, we use nine RAMIP models to quantify the aerosol ERF associated with global aerosol reductions, as well as regional aerosol reductions from four regions and the rest of the world. Our rest of the world signal assumes linearity, as it is estimated as the difference between global aerosol reductions and the sum of the four regional aerosol reductions. We decompose the aerosol ERF into ERF_{ari} and ERF_{aci} components, as well as their subcomponents (e.g. scattering versus absorbing). Section 2 briefly summarizes the RAMIP experimental design and models, and also describes the ERF decomposition methodology. Section 3 presents results, including the global mean ERF decomposition for the global aerosol perturbation, the four regional aerosol perturbations and the corresponding difference (i.e. rest of the world). Conclusions and discussion follow in section 4.

2. Data and methods

2.1. Model experiments

Following protocols from the Radiative Forcing Model Intercomparison Project (RFMIP), we use pairs of climate model simulations with sea surface temperatures (SSTs), sea ice concentrations (SICs) and land use fixed to preindustrial monthly climatologies and integrated for 30 years (table 1) (Pincus *et al* 2016, Wilcox *et al* 2023). As ERF is weakly dependent on the background state (Forster *et al* 2016, Pincus *et al* 2016), the exact choice of background SST and sea ice has little impact of the ERF. All simulations feature year 2050 GHGs, ozone and natural aerosol and precursor gas emissions from SSP3-7.0. The baseline experiment (piClim-370) also uses year 2050 AA and precursor gas emissions from SSP3-7.0, which features weak levels of air quality control. The global aerosol reduction experiment (i.e. piClim-370-126aer) is identical in all ways except it uses year 2050 AA and precursor gas emissions from SSP1-2.6, which features strong levels of air quality control. The regional aerosol reduction experiments (e.g. piClim-370-EAS126aer) also use year 2050 AA and precursor gas emissions from SSP1-2.6 within the region of consideration (e.g. East Asia (EAS)) and SSP3-7.0 emissions otherwise. In all cases, 'AA and precursor gas emissions' includes both industrial and biomass burning emissions of sulfur dioxide (SO_2), sulfate (SO_4), BC, and OA. We note that the bulk of the emissions decrease is due to industrial (as opposed to biomass burning) emissions. For GLO, for example, 99% of the decrease in SO_2 emissions is due to industrial emissions. The corresponding percentages for OA and BC are 84% and 97%, respectively. The seasonal cycle of emissions is included in all simulations. The corresponding aerosol reduction signals are obtained by subtracting the baseline piClim-370 experiment from each of the aerosol reduction experiments. GLO refers to the global aerosol reduction signal; AFR refers to the Africa and Middle East aerosol reduction signal; EAS refers to the EAS aerosol reduction signal; NAE refers to the North America and Europe (NAE) aerosol reduction signal; and South Asia (SAS) refers to the South Asia aerosol reduction signal. Assuming linearity, we also approximate the rest of the world signal as GLO minus the sum of the four regions. The rest of the world includes regions such as South America, Central America, Australia, Russia and Indonesia.

Table 1. RAMIP fixed SST experiments. All experiments are integrated for 30 years and use preindustrial SSTs, sea ice extent, and land use. Anthropogenic emissions are for the year 2050 and include the seasonal cycle. Africa and the Middle East is the region bounded by 35° S, 35° N, 20° W, and 60° E; East Asia is the region bounded by 20 and 53° N and 95 and 133°E; North America and Europe are the regions bounded by 35°N, 70°N, 20°W, and 45°E and 25°N, 70°N, 150°W, and 45°W; and South Asia is the region bounded by 5 and 35°N and 65 and 95°E. In all cases, 'anthropogenic aerosol and precursor gas emissions' includes both industrial and biomass burning emissions of sulfur dioxide (SO_2), sulfate (SO_4), black carbon (BC), and organic aerosol (OA).

Experiment	GHGs, ozone and natural emissions	Anthropogenic aerosol and precursor gas emissions	Aerosol Reduction Signal
piClim-370	SSP3-7.0	SSP3-7.0	N/A
piClim-370-126aer	SSP3-7.0	SSP1-2.6	GLO = piClim-370-126aer minus piClim-370
piClim-370-AFR126aer	SSP3-7.0	SSP1-2.6 within the Africa and Middle East region, SSP3-7.0 otherwise	AFR = piClim-370-AFR126aer minus piClim-370
piClim-370-EAS126aer	SSP3-7.0	SSP1-2.6 within the East Asia region, SSP3-7.0 otherwise	EAS = piClim-370-EAS 126aer minus piClim-370
piClim-370-NAE126aer	SSP3-7.0	SSP1-2.6 within the North America and Europe region, SSP3-7.0 otherwise	NAE = piClim-370-NAE126aer minus piClim-370
piClim-370-SAS126aer	SSP3-7.0	SSP1-2.6 within the South Asia region, SSP3-7.0 otherwise	SAS = piClim-370-SAS126aer minus piClim-370

Table 2. RAMIP models and their atmospheric resolution, aerosol scheme, aerosol indirect effects considered, RAMIP data reference and model reference.

Model	Atmos. Res.	Aerosol Scheme	Indirect Effects	RAMIP Data Reference	Model Reference
CNRM-ESM2-1	1.4° × 1.4°	TACTIC v2 (modal)	Twomey effect only	Nabat (2025)	Seferian *et al* (2019)
GFDL-SPEAR_LO	1° × 1.25°	AM4 aerosol (bulk)	Twomey and Albrecht effects	Paynter (2025)	Delworth *et al* (2020)
MIROC6	1.4° × 1.4°	SPRINTARS 6.0 (bulk)	Twomey and Albrecht effects	Takemura (2025)	Tatebe *et al* (2019)
NorESM2-LM	1.9° × 2.5°	OsloAero (modal)	Twomey and Albrecht effects	Lewinschal (2025)	Seland *et al* (2020)
CESM2	1.9° × 2.5°	MAM4 (modal)	Twomey and Albrecht effects	Allen (2025)	Danabasoglu *et al* (2020)
EC-Earth3-AerChem	0.7° × 0.7°	TM5 (bulk)	Twomey and Albrecht effects	O'Donnell *et al* (2025)	van Noije *et al* (2021)
GISS-E2-1-G	2° × 2.5°	OMA (bulk)	Twomey effect only	Westervelt *et al* (2025)	Kelley *et al* (2020)
MRI-ESM2-0	1.125° × 1.125°	MASINGAR mk2r4 (bulk)	Twomey and Albrecht effects	Oshima and Koshiro (2025)	Yukimoto *et al* (2019)
UKESM1-0-LL	1.25° × 1.875°	GLOMAP-mode (modal)	Twomey and Albrecht effects	Rumbold *et al* (2025)	Sellar *et al* (2019)

2.2. Models

Nine RAMIP models performed the fixed SST simulations and archived the required variables for this analysis. Models include CESM2, GFDL-SPEAR_LO, CNRM-ESM2-1, MRI-ESM2-0, EC-Earth3-AerChem, NorESM2-LM, GISS-E2-1-G, UKESM1-0-LL and MIROC6 (table 2). All nine models include an interactive representation of aerosols (e.g. transport, removal). Seven models include a representation of both aerosol-cloud indirect effects. CNRM-ESM2-1 and GISS-E2-1-G lack the Albrecht effect (table 2). All model data is reinterpolated to a 2.5° × 2.5° grid. Analyses are based on all 30 years of the fixed SST experiments.

2.3. ERF decomposition

The total change in net TOA radiation between the baseline experiment (piClim-370) and an aerosol-perturbed experiment (e.g. piClim-370-126aer), both with fixed SSTs and SICs (Forster *et al* 2016), can be expressed as:

$$\Delta R = \mathrm{ERF}_{\mathrm{ari}} + \mathrm{ERF}_{\mathrm{aci}} + \Delta R_{\mathrm{albedo}} + \Delta R_{\mathrm{To}}. \quad (1)$$

$\mathrm{ERF}_{\mathrm{ari}}$ is the ERF due to aerosol-radiation interactions. As defined in IPCC AR6, this includes the instantaneous radiative forcing, non-cloud atmospheric adjustments (temperature and water vapor) and

cloud adjustments due to changes in the thermal structure of the atmosphere caused by absorbing aerosols, i.e. the semi-direct effect (Forster *et al* 2021). $\mathrm{ERF_{aci}}$ is the ERF due to aerosol-cloud interactions, which includes the instantaneous radiative forcing due to changes in cloud liquid and ice particle number concentrations and sizes, and adjustments of cloud water and coverage (Forster *et al* 2021). $\Delta R_{\mathrm{albedo}}$ and ΔR_{To} represent the change in TOA radiation due to the change in surface albedo and surface temperature, respectively.

Equation (1) can be decomposed into shortwave (SW) and longwave (LW) components:

$$\Delta R^{\mathrm{SW}} = \mathrm{ERF}^{\mathrm{SW}}_{\mathrm{ari}} + \mathrm{ERF}^{\mathrm{SW}}_{\mathrm{aci}} + \Delta R^{\mathrm{SW}}_{\mathrm{albedo}}, \tag{2}$$

$$\Delta R^{\mathrm{LW}} = \mathrm{ERF}^{\mathrm{LW}}_{\mathrm{ari}} + \mathrm{ERF}^{\mathrm{LW}}_{\mathrm{aci}} + \Delta R^{\mathrm{LW}}_{\mathrm{To}}. \tag{3}$$

The approximate partial radiative perturbation (APRP) method (Taylor *et al* 2007, Zelinka *et al* 2014, 2023) can be used to derive estimates of the SW terms in equation (2), and has been shown to yield accurate estimates that are comparable to those obtained from double radiation calls (Ghan *et al* 2013). APRP is used to decompose SW $\mathrm{ERF_{ari}}$ into non-cloud scattering and non-cloud absorbing components:

$$\mathrm{ERF}^{\mathrm{SW}}_{\mathrm{ari}} = \mathrm{ERF}^{\mathrm{SW}}_{\mathrm{ari,scat}} + \mathrm{ERF}^{\mathrm{SW}}_{\mathrm{ari,abs}}. \tag{4}$$

APRP is also used to decompose SW $\mathrm{ERF_{aci}}$ into cloud scattering, cloud absorbing and cloud amount components:

$$\mathrm{ERF}^{\mathrm{SW}}_{\mathrm{aci}} = \mathrm{ERF}^{\mathrm{SW}}_{\mathrm{aci,scat}} + \mathrm{ERF}^{\mathrm{SW}}_{\mathrm{aci,abs}} + \mathrm{ERF}^{\mathrm{SW}}_{\mathrm{aci,amt}}. \tag{5}$$

As discussed in Zelinka *et al* (2023), APRP provides estimates of $\mathrm{ERF^{SW}}$ that are made up of slightly different component groupings than the IPCC AR6 definition–in particular, APRP's direct effect (equation (4)) equals IPCC's direct effect minus the semi-direct effect, whereas APRP's indirect effect (equation (5)) equals IPCC's indirect effect plus the semi-direct effect (i.e. the semi-direct effect in our analysis is an indirect effect). Nonetheless, the sum of the direct and indirect SW effects is the same under IPCC AR6 and APRP.

The LW terms in equation (3) can be estimated with proxies (Zelinka *et al* 2014, 2023, Smith *et al* 2020) according to:

$$\mathrm{ERF}^{\mathrm{LW}}_{\mathrm{ari}} = \Delta R^{\mathrm{LW}}_{\mathrm{cs}} - \Delta R^{\mathrm{To}}_{\mathrm{cs}}, \tag{6}$$

where $\Delta R^{\mathrm{LW}}_{\mathrm{cs}}$ is the change in TOA clear-sky LW radiative flux and $\Delta R^{\mathrm{To}}_{\mathrm{cs}}$ is the change in TOA clear-sky LW radiative flux associated with the changes in land surface temperature. The latter term in equation (6) is estimated by multiplying the clear-sky surface temperature radiative kernel by the change in surface temperature (Zelinka *et al* 2023) according to:

$$\Delta R^{\mathrm{To}}_{\mathrm{cs}} = K^{\mathrm{To}}_{\mathrm{cs}} \times \Delta T_{\mathrm{o}} \tag{7}$$

$K^{\mathrm{To}}_{\mathrm{cs}}$ is estimated using a Python-based radiative kernel tool kit and the Geophysical Dynamics Laboratory radiative kernel (Soden *et al* 2008, Smith *et al* 2018). The LW $\mathrm{ERF_{aci}}$ in equation (3) is likewise estimated using a proxy, as the change in LW cloud radiative effect:

$$\mathrm{ERF}^{\mathrm{LW}}_{\mathrm{aci}} = \Delta\mathrm{CRE}^{\mathrm{LW}} = \Delta R^{\mathrm{LW}} - \Delta R^{\mathrm{LW}}_{\mathrm{cs}}, \tag{8}$$

where ΔR^{LW} is the change in TOA all-sky LW radiative flux and $\Delta R^{\mathrm{LW}}_{\mathrm{cs}}$ is the previously defined change in TOA clear-sky LW radiative flux. As discussed in Zelinka *et al* (2023), this proxy for the LW direct effect (equation (6)) equals IPCC's direct effect minus the semi-direct effect minus masking terms which quantify how much the radiative impact of changes in temperature, humidity, and aerosols is attenuated by clouds. This proxy for the LW indirect effect (equation (8)) equals IPCC's indirect effect plus the semi-direct effect plus the aforementioned masking terms, i.e. the semi-direct effect plus masking terms in our analysis is an indirect effect.

Global multimodel mean maps of the SW albedo term ($\Delta R^{\mathrm{SW}}_{\mathrm{albedo}}$) and the LW surface temperature term ($\Delta R^{\mathrm{LW}}_{\mathrm{To}}$) for each aerosol reduction signal are included in supplementary figures 1 and 2. Multimodel mean global mean values of $\Delta R^{\mathrm{SW}}_{\mathrm{albedo}}$ and $\Delta R^{\mathrm{LW}}_{\mathrm{To}}$ are all relatively small for each aerosol reduction signal, with limited significance (supplementary table 1).

3. Results

3.1. Aerosol optical depth responses

Although the magnitude of the aerosol reduction is important to the overall ERF, the type of aerosol species is also important. Reductions in BC, for example, can act to offset reductions in SO_4 by muting aerosol-radiation interactions. SO_4 is also a much more efficient CCN than most other AA species, which will have disproportionate impacts on aerosol-cloud interactions. Furthermore, the region where the aerosol emissions reduction occurs is also important, due to factors such as underlying surface brightness (i.e. albedo), background climate which can impact transport and removal, as well as other environmental factors including the dominant cloud regimes, which impact aerosol-cloud interactions. The background levels of air pollution can also contribute to nonlinear aerosol-cloud interactions, which become saturated in more polluted regions with higher background aerosol (e.g. Jia and Quaas 2023).

Aerosol optical depth (AOD; here at 550 nm) is a measure of the extinction (e.g. scattering and absorption) of the solar beam due to aerosols. We use it here to provide a broad overview of the aerosol reduction signals across RAMIP experiments. Figure 1 shows the multimodel mean annual mean AOD response for the sum of AAs including sulfate, BC and OA (abbreviated as AAOD). As expected, all aerosol reduction signals yield global mean decreases in AAOD. For example, GLO yields the largest reductions of $-21.8 \pm 6.4\ 10^{-3}$. This is followed by EAS, SAS, AFR and NAE at $-5.4 \pm 1.6\ 10^{-3}$, $-4.9 \pm 1.4\ 10^{-3}$, $-3.8 \pm 0.8\ 10^{-3}$, $-2.2 \pm 0.9\ 10^{-3}$, respectively (table 3). A similar ranking also occurs based on AA emissions (SSP1-2.6 minus SSP3-7.0 in the year 2050), with GLO yielding the largest emissions reductions at -100.4 Tg year^{-1}, followed by EAS, SAS, AFR and NAE at -29.0, -20.8, -12.4 and -10.7 Tg year^{-1}, respectively (table 3).

The regional aerosol emission signals show maximum AAOD decreases centered over the region of emission reduction, but with remote dispersion due to long range transport. Emission reduction regions in the Northern Hemisphere (NH), including EAS, NAE and SAS (figures 1(c)–(e)), show AAOD reductions throughout most of the NH. In contrast, minimal AAOD reductions occur in the Southern Hemisphere, indicating small cross equatorial transport. AFR emission reductions, which occur on both sides of the equator, yield AAOD responses in both hemispheres (figure 1(b)). We note the AAOD increase near southern Africa under GLO and AFR (figures 1(a) and (b)), which is largely due to increases in SO_4 AOD (as well as OA AOD; supplementary figures 3–5). This is associated with industrialization and infrastructure expansion in the near-term, along with continued reliance on fossil fuels for energy, industry, and transportation. Weak increases in biomass burning emissions also contribute here (emissions maps for SSP1-2.6 minus SSP3-7.0 in the year 2050 are included in supplementary figure 6).

Table 3 also shows the corresponding statistics separately for SO_4 AOD, OA AOD and BC AOD (maps are provided in supplementary figures 3–5). About half of the GLO AAOD decrease is associated with SO_4 AOD at 53%, as compared with OA AOD (34%) and BC AOD (13%). Similar values are obtained for EAS, where the AAOD decrease is largely associated with SO_4 AOD at 52%, as compared with OA AOD (33%) and BC AOD (15%). Similar statements also apply for SAS, where SO_4 AOD accounts for 59% of the AAOD decrease, followed by OA AOD at 31% and BC AOD at 10%. An even larger percentage of the NAE AAOD decrease is associated with SO_4 AOD at 73% (20% for OA AOD) with small contributions from BC AOD at 7%. In contrast, a relatively small percentage of the AFR AAOD decrease is associated with SO_4 AOD at 36%, with relatively large contributions from OA AOD at 43% and BC AOD at 21%.

Thus, the global mean AAOD decrease for GLO, EAS and SAS is dominated by SO_4 AOD (more than 50% of the total). This percentage is even higher for NAE at 73%. For AFR, the BC AOD decrease represents 21% of the AAOD decrease, which is the largest relative contribution from BC. In contrast, the AFR SO_4 AOD decrease represents only 36% of the AAOD decrease, which is the smallest relative contribution from SO_4. Although the percentages are different, analogous statements exist based on emissions, including the relatively large SO_2 contribution to NAE emissions reductions and the relatively large BC contribution to AFR emissions reductions. These proportional aerosol species differences are due to different emission sources, and in particular, the larger importance of biomass burning aerosol (largely BC and OA) for AFR. In subsequent sections, we use this AOD analysis to better understand the ERF responses across RAMIP experiments.

3.2. ERF decomposition for global aerosol reduction

Figure 2 shows the global mean ERF decomposition based on the global aerosol reduction signal. Bars represent the multimodel mean and error bars show the ± 1 standard deviation across models. Individual

Table 3. Multimodel mean global mean aerosol optical depth (AOD) and emissions statistics. Rows show the AOD response based on sulfate aerosol (SO_4 AOD); organic aerosol (OA AOD); black carbon (BC AOD); and their sum (AAOD). Columns show the aerosol reduction signals, including the sum of the four regions (EAS + NAE + SAS + AFR). Uncertainty is quantified as the intermodal spread (±1 standard deviations across the models). Bold values indicate that the spread does not encompass 0 (accounting for roundoff). All AOD units are 10^{-3}. Only 6 models are available for this analysis, including CESM2, CNRM-ESM2-1, EC-Earth3-AerChem, MIROC6, MRI-ESM2-0 and NorESM2-LM. Also included are corresponding statistics based on total (industrial + biomass burning) emissions of SO_2, BC and OA (SSP1-2.6 minus SSP3-7.0 for the year 2050), as well as decomposition into industrial versus biomass burning emissions. Units are Tg $year^{-1}$.

ΔAOD	GLO	EAS	NAE	SAS	AFR	EAS + NAE + SAS + AFR
SO_4	**−11.6 ± 4.2**	**−2.8 ± 1.0**	**−1.6 ± 0.7**	**−2.9 ± 1.2**	**−1.4 ± 0.4**	**−8.7 ± 1.8**
OA	**−7.5 ± 3.1**	**−1.8 ± 0.7**	**−0.5 ± 0.2**	**−1.5 ± 0.5**	**−1.7 ± 0.6**	**−5.4 ± 1.1**
BC	**−2.7 ± 1.5**	**−0.8 ± 0.5**	**−0.2 ± 0.1**	**−0.5 ± 0.2**	**−0.8 ± 0.4**	**−2.2 ± 0.7**
AA	**−21.8 ± 6.4**	**−5.4 ± 1.6**	**−2.2 ± 0.9**	**−4.9 ± 1.4**	**−3.8 ± 0.8**	**−16.3 ± 2.4**
Δ Emissions (Total)	GLO	EAS	NAE	SAS	AFR	EAS + NAE + SAS + AFR
SO_2	−72.9	−20.9	−9.3	−16.3	−5.9	−52.4
OA	−20.2	−5.6	−1.0	−3.4	−4.7	−14.7
BC	−7.3	−2.5	−0.4	−1.1	−1.8	−5.8
AA	−100.4	−29.0	−10.7	−20.8	−12.4	−72.9
Δ Emissions (Industrial)	GLO	EAS	NAE	SAS	AFR	EAS + NAE + SAS + AFR
SO_2	−72.4	−20.8	−9.2	−16.2	−6.2	−52.4
OA	−16.9	−5.1	−0.7	−3.3	−5.5	−14.6
BC	−7.1	−2.45	−0.4	−1.07	−2.0	−5.9
AA	−96.4	−28.3	−10.3	−20.6	−13.7	−72.9
Δ Emissions (Biomass)	GLO	EAS	NAE	SAS	AFR	EAS + NAE + SAS + AFR
SO_2	−0.47	−0.11	−0.05	−0.04	0.25	0.05
OA	−3.3	−0.5	−0.3	−0.1	0.9	−0.04
BC	−0.26	−0.04	−0.02	−0.02	0.14	0.06
AA	−4.0	−0.68	−0.36	−0.18	1.28	0.07

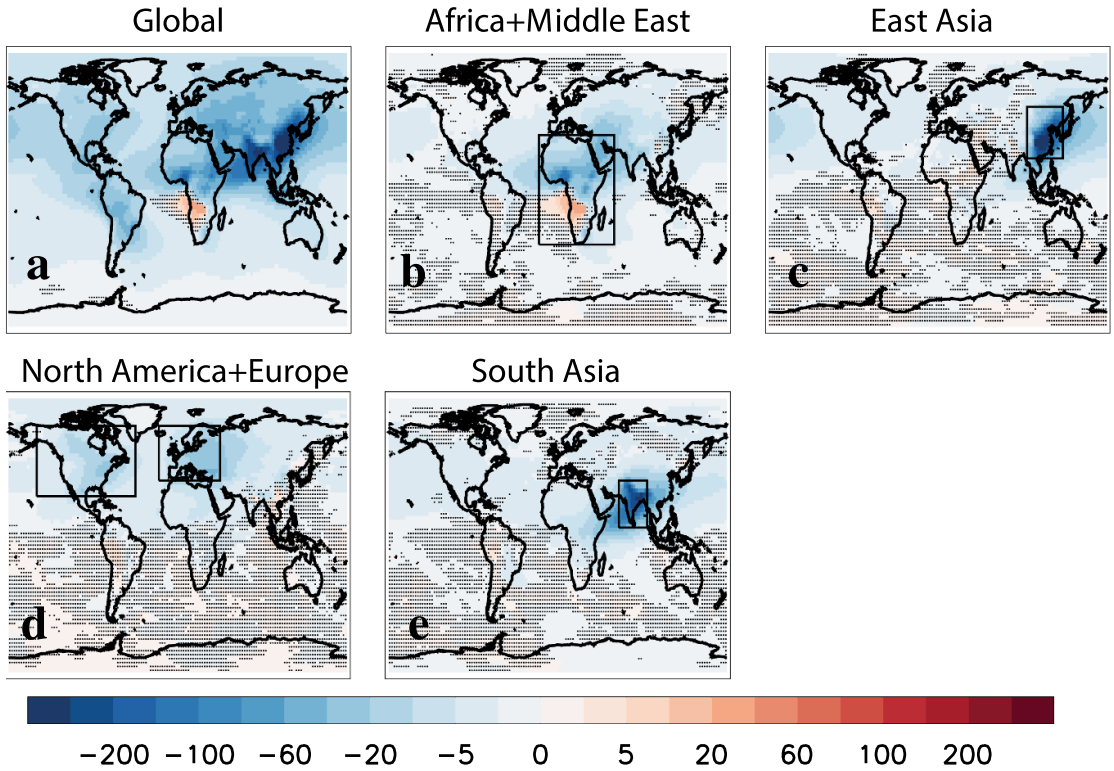

Figure 1. Spatial maps of the multimodel mean aerosol optical depth response. AOD is based on the sum of sulfate AOD + organic aerosol AOD + black carbon AOD (AAOD). Panels show the (a) Global; (b) Africa + Middle East; (c) East Asia (d) North America + Europe; and (e) South Asia aerosol reduction signal. Only 6 models are available for this analysis, including CESM2, CNRM-ESM2-1, EC-Earth3-AerChem, MIROC6, MRI-ESM2-0 and NorESM2-LM. Non-stippled regions indicate grid boxes where at least 5 out of the 6 models agree on the sign. Black boxes designate boundaries for the four RAMIP regions. Units are 10^{-3}.

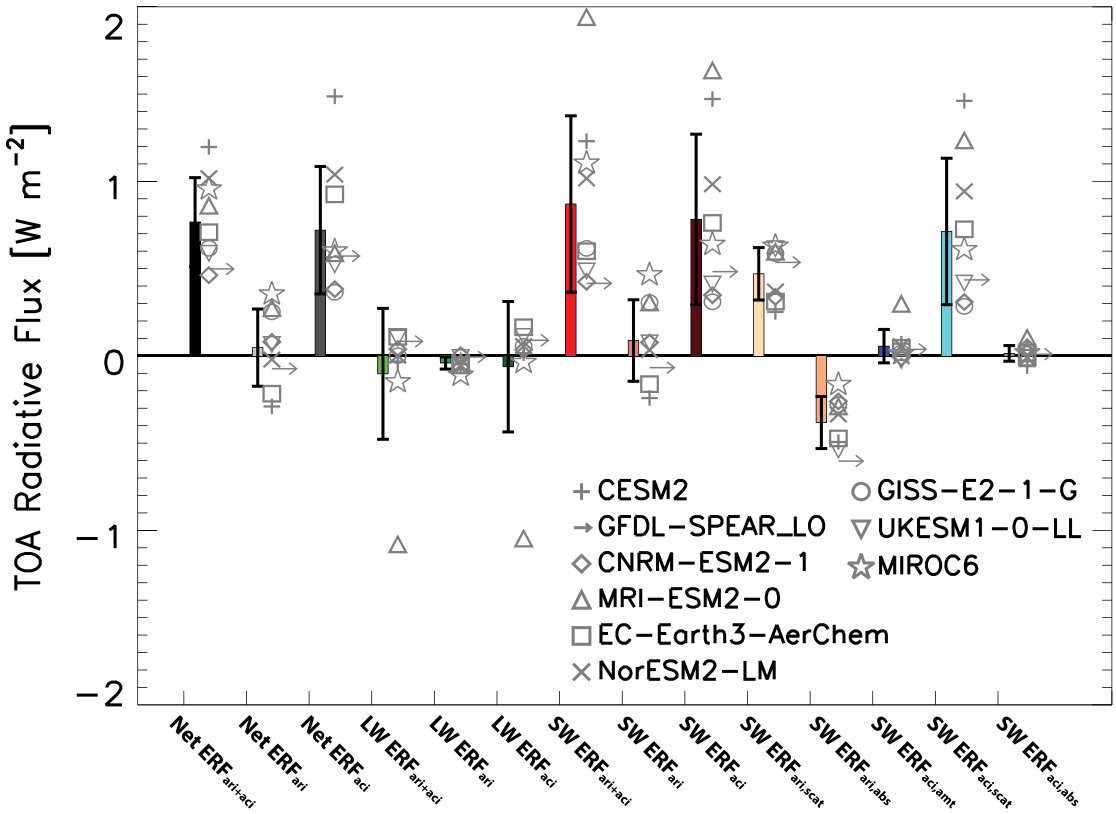

Figure 2. Global mean ERF decomposition bar chart for the global aerosol reduction signal. Bars show the global mean multimodel mean ERF decomposition, with the corresponding error bars representing the intermodal spread (±1 standard deviations across the models). Gray symbols show individual model results. Units are W m^{-2}.

model results are also included as gray symbols. As expected, a relatively large and significant positive net ERF$_{ari+aci}$ exists at 0.77 ± 0.25 W m^{-2} (see also table 4 and supplementary figure 7). This corresponds to about 71% of the magnitude of the historical (2015 relative to 1850) net ERF$_{ari+aci}$ from a larger collection (>20) of models (Zelinka *et al* 2023) participating in the Coupled Model Intercomparison Project version 6 (CMIP6; Eyring *et al* 2016). Although all nine models yield a positive net ERF$_{ari+aci}$, the intermodal spread is relatively large at 0.46 W m^{-2} for CNRM-ESM2-1–1.20 W m^{-2} for CESM2. Nearly all of the net ERF$_{ari+aci}$ increase is associated with net ERF$_{aci}$ at 0.72 ± 0.37 W m^{-2} which corresponds to about 82% of the historical net ERF$_{aci}$ from Zelinka *et al* (2023). All nine models yield a positive value, with the largest increase for CESM2 and NorESM2-LM (as for net ERF$_{ari+aci}$). The two models (CNRM-ESM2-1 and GISS-E2-1-G) that lack the Albrecht effect (table 2) yield the weakest net ERF$_{aci}$ increase. The contribution from net ERF$_{ari}$ is much smaller and not significant at 0.05 ± 0.22 W m^{-2} (24% of the historical value). The intermodel spread for net ERF$_{ari}$ spans both negative (e.g. CESM2 and EC-Earth3-AerChem) and positive values (MIROC6, GISS-E2-1-G and MRI-ESM2-0).

The increase in net ERF$_{ari+aci}$ is due to SW ERF$_{ari+aci}$ at 0.87 ± 0.51 W m^{-2} which is weakly muted by LW ERF$_{ari+aci}$ at −0.10 ± 0.38 W m^{-2}. The latter, however, is heavily influenced by a relatively large negative value of −1.08 W m^{-2} in MRI-ESM2-0, which in turn is due to a relatively large negative value of LW ERF$_{aci}$. As highlighted by Smith *et al* (2020), this is due to ice cloud nucleation by BC aerosols (which here are decreasing) in high-level tropical clouds with temperature below −38 °C (Oshima *et al* 2020). Although three other models (CESM2, MIROC6, and NorESM2-LM) also include aerosol interactions on ice clouds (significant in the LW), they yield small (and in some cases positive) LW ERF$_{aci}$.

SW ERF$_{ari+aci}$ is largely due to SW ERF$_{aci}$ at 0.78 ± 0.49 W m^{-2}. All nine models yield a positive value, but again with large spread (0.31 W m^{-2} in GISS-E2-1-G to 1.64 W m^{-2} in MRI-ESM2-0). As before, both GISS-E2-1-G and CNRM-ESM2-1 yield the smallest increase. For MRI-ESM2-0, the aforementioned large negative LW ERF$_{aci}$ is largely offset by a large positive SW ERF$_{aci}$. In terms of SW aerosol-radiation interactions, SW ERF$_{ari}$ is relatively weak and not significant at 0.09 ± 0.23 W m^{-2}. This is due to opposing SW ERF$_{ari,scat}$ at 0.48 ± 0.15 W m^{-2} and SW ERF$_{ari,abs}$ at −0.38 ± 0.15 W

Table 4. Multimodel mean global mean statistics for the ERF decomposition. Uncertainty is quantified as the intermodal spread (±1 standard deviations across the models). Bold values indicate that the spread does not encompass 0 (accounting for roundoff). All ERF units are W m^{-2}. Also included is normalized net $ERF_{ari+aci}$ (units of W m^{-2} per AAOD) where $ERF_{ari+aci}$ is divided by the absolute value of the change in AAOD. Corresponding normalized net $ERF_{ari+aci}$ (units of W m^{-2} per Tg $year^{-1}$) are also included, where $ERF_{ari+aci}$ is divided by the absolute value of the change in AA emissions.

ERFs	GLO	EAS	NAE	SAS	AFR
Net $ERF_{ari+aci}$	**0.77 ± 0.25**	**0.15 ± 0.07**	**0.13 ± 0.09**	**0.10 ± 0.05**	0.05 ± 0.07
Net ERF_{ari}	0.05 ± 0.22	−0.01 ± 0.06	0.03 ± 0.04	0.04 ± 0.05	**−0.06 ± 0.05**
Net ERF_{aci}	**0.72 ± 0.37**	**0.16 ± 0.10**	**0.11 ± 0.08**	**0.06 ± 0.06**	**0.11 ± 0.08**
LW $ERF_{ari+aci}$	−0.10 ± 0.38	−0.004 ± 0.05	−0.01 ± 0.05	0.002 ± 0.06	0.004 ± 0.11
LW ERF_{ari}	**−0.04 ± 0.04**	−0.002 ± 0.02	−0.01 ± 0.03	−0.01 ± 0.01	−0.01 ± 0.01
LW ERF_{aci}	−0.06 ± 0.37	−0.001 ± 0.06	−0.01 ± 0.03	0.01 ± 0.05	0.01 ± 0.11
SW $ERF_{ari+aci}$	**0.87 ± 0.51**	**0.16 ± 0.09**	**0.15 ± 0.08**	**0.10 ± 0.08**	0.04 ± 0.11
SW ERF_{ari}	0.09 ± 0.23	−0.01 ± 0.06	**0.04 ± 0.02**	0.05 ± 0.05	**−0.05 ± 0.05**
SW ERF_{aci}	**0.78 ± 0.49**	**0.16 ± 0.10**	**0.11 ± 0.09**	**0.05 ± 0.06**	**0.10 ± 0.09**
SW $ERF_{ari,scat}$	**0.47 ± 0.15**	**0.10 ± 0.03**	**0.06 ± 0.02**	**0.12 ± 0.04**	**0.07 ± 0.02**
SW $ERF_{ari,abs}$	**−0.38 ± 0.15**	**−0.11 ± 0.04**	**−0.02 ± 0.02**	**−0.07 ± 0.03**	**−0.12 ± 0.04**
SW $ERF_{aci,amt}$	0.06 ± 0.10	0.02 ± 0.02	0.02 ± 0.04	−0.01 ± 0.03	0.001 ± 0.04
SW $ERF_{aci,scat}$	**0.71 ± 0.42**	**0.14 ± 0.09**	**0.10 ± 0.08**	**0.06 ± 0.05**	**0.09 ± 0.08**
SW $ERF_{aci,abs}$	0.01 ± 0.05	0.01 ± 0.01	0.000 ± 0.004	0.002 ± 0.01	0.003 ± 0.01
Normalized ERFs (by AAOD)	GLO	EAS	NAE	SAS	AFR
Net $ERF_{ari+aci}$	35.3	27.8	59.1	20.4	13.2
Normalized ERFs (by emissions)	GLO	EAS	NAE	SAS	AFR
Net $ERF_{ari+aci}$	0.0077	0.0052	0.0121	0.0048	0.0040

m^{-2}. The opposing non-cloud scattering and non-cloud absorption is consistent with the decrease in scattering (SO_4) and absorbing BC aerosols (table 3).

Finally, SW ERF_{aci} is dominated by SW $ERF_{aci,scat}$ at 0.71 ± 0.42 W m^{-2}. All nine models yield a positive value, but with a large range of 0.28 W m^{-2} (GISS-E2-1-G) to 1.46 W m^{-2} (CESM2). The other SW cloud terms including SW $ERF_{aci,amt}$ and SW $ERF_{aci,abs}$ are both small and not significant at 0.06 ± 0.10 W m^{-2} and 0.01 ± 0.05 W m^{-2}, respectively. To summarize, nearly all (94%) of the increase in net $ERF_{ari+aci}$ is due to aerosol-cloud interactions, which in turn is largely associated with reduced SW cloud scattering.

3.3. ERF decomposition for EAS aerosol reduction

A significant increase in net $ERF_{ari+aci}$ for EAS exists at 0.15 ± 0.07 W m^{-2} (table 4; see also supplementary figures 8 and 9). Of the four regional perturbations, EAS yields the largest increase in net $ERF_{ari+aci}$, which corresponds to about 19% of the increase in net $ERF_{ari+aci}$ under global aerosol reductions. All nine models yield an increase, with once again a relatively large range that spans 0.06 W m^{-2} (SPEAR) to 0.24 W m^{-2} (CESM2). The conclusions discussed above in section 3.2 for the global aerosol reduction also apply here. This includes the importance of aerosol-cloud interactions and in particular, SW $ERF_{aci,scat}$ at 0.14 ± 0.09 W m^{-2}. Here, aerosol-radiation interactions are weakly negative at −0.01 ± 0.06 W m^{-2}, with five models yielding a negative value and four models yielding a positive value. As in GLO, the weak net ERF_{ari} is due to opposing changes in SW $ERF_{ari,scat}$ at 0.10 ± 0.03 W m^{-2} versus SW $ERF_{ari,abs}$ at −0.11 ± 0.04 W m^{-2}. Thus, aerosol-cloud interactions dominate the EAS net $ERF_{ari+aci}$, largely due to reduced SW cloud scattering. Aerosol-radiation interactions are small (weakly negative) and not significant, due to similar magnitude increases in non-cloud scattering and decreases in non-cloud absorption.

3.4. ERF decomposition for NAE aerosol reduction

A significant increase in net $ERF_{ari+aci}$ for NAE exists at 0.13 ± 0.09 W m^{-2} (table 4; see also supplementary figures 10 and 11). This represents the second largest increase in net $ERF_{ari+aci}$ across the four regional aerosol reduction signals, and corresponds to about 17% of the increase in net $ERF_{ari+aci}$ under global aerosol reductions. All nine models yield an increase, but with relatively large range (0.01 W m^{-2} in CNRM-ESM2-1–0.30 W m^{-2} in CESM2). As with GLO and EAS, net $ERF_{ari+aci}$ is dominated by aerosol-cloud interactions and in particular, SW $ERF_{aci,scat}$ at 0.10 ± 0.08 W m^{-2}. Net ERF_{ari} is weakly positive at 0.03 ± 0.04 W m^{-2} which is related to SW $ERF_{ari,scat}$ at 0.06 ± 0.02 W m^{-2} dominating

over SW $ERF_{ari,abs}$ at -0.02 ± 0.02 W m^{-2}. This is in general consistent with the larger contribution of SO_4 (as opposed to BC) to the total NAE aerosol decrease, i.e. SO_4 AOD comprises 73% of the AAOD decrease. Thus, aerosol-cloud interactions dominate net $ERF_{ari+aci}$ for NAE, largely due to reduced SW cloud scattering. Aerosol-radiation interactions also contribute to the overall positive $ERF_{ari+aci}$, due to a relatively large positive contribution from non-cloud scattering.

3.5. ERF decomposition for South Asia aerosol reduction

A significant increase in net $ERF_{ari+aci}$ SAS exists at 0.10 ± 0.05 W m^{-2} (table 4; see also supplementary figures 12 and 13). This represents the third largest increase in net $ERF_{ari+aci}$ across the four regional aerosol reduction signals, and corresponds to about 13% of the increase in net $ERF_{ari+aci}$ under global aerosol reductions. All nine models yield an increase, but with a relatively large range at 0.03 W m^{-2} in CNRM-ESM2-1–0.15 W m^{-2} in CESM2. The conclusions discussed above also apply here. This includes the importance of net ERF_{aci} at 0.06 ± 0.06 W m^{-2} and in particular SW $ERF_{aci,scat}$ at 0.06 ± 0.05 W m^{-2}. In terms of aerosol-radiation interactions, SAS net ERF_{ari} is the largest of the four regions at 0.04 ± 0.05 W m^{-2} which is due to SW $ERF_{ari,scat}$ at 0.12 ± 0.04 W m^{-2} dominating over SW $ERF_{ari,abs}$ at -0.07 ± 0.02 W m^{-2}. This is in general consistent with the relatively large contribution of SO_4 to the total AAOD decrease (59% of the total) as compared to BC (10% of the total). Thus, aerosol-cloud interactions still dominate for SAS, but aerosol-radiation interactions also contribute to the overall positive net $ERF_{ari+aci}$, largely due to a relatively large positive contribution from non-cloud scattering.

3.6. ERF decomposition for Africa and middle East aerosol reduction

Unlike the other regional signals, a non-significant increase in net $ERF_{ari+aci}$ exists for AFR at 0.05 ± 0.07 W m^{-2} (table 4; see also supplementary figures 14 and 15). This represents the weakest increase in net $ERF_{ari+aci}$ across the four regional aerosol reduction signals, and corresponds to about 6% of the increase in net $ERF_{ari+aci}$ under global aerosol reductions. Six models yield an increase and three yield a decrease. The range spans -0.02 W m^{-2} in MRI-ESM2-0–0.17 W m^{-2} in MIROC6. Although net ERF_{aci} remains most important at 0.11 ± 0.08 W m^{-2}, AFR has the largest negative (and significant) net ERF_{ari} at -0.06 ± 0.05 W m^{-2}. SW $ERF_{aci,scat}$ remains the dominant driver of ERF_{aci} at 0.09 ± 0.08 W m^{-2}. The relatively large negative net ERF_{ari} is due to SW $ERF_{ari,abs}$ at -0.12 ± 0.04 W m^{-2} dominating over SW $ERF_{ari,scat}$ at 0.07 ± 0.02 W m^{-2}. This is in general consistent with the relatively large contribution of BC to the total aerosol decrease, i.e. BC AOD comprises 21% of the AAOD decrease, which is the largest of our four regions. AFR also yields a relatively small decrease in SO_4 at 36% of the total AAOD decrease. Thus, aerosol-cloud interactions still dominate for AFR, but with larger cancellation from aerosol-radiation interactions, due to a relatively large negative contribution from non-cloud absorption.

3.7. Normalized ERFs

As mentioned above, the global mean NAE net $ERF_{ari+aci}$ is nearly as large as that for EAS (0.13 ± 0.09 versus 0.15 ± 0.07 W m^{-2}). This is despite smaller NAE decreases in AAOD at -2.2 ± 0.9 10^{-3} relative to EAS at -5.4 ± 1.6 10^{-3} (table 3). This is more clearly shown by normalizing net $ERF_{ari+aci}$ by the absolute value of the change in AAOD, which yields a forcing efficiency of 27.8 W m^{-2} per AAOD for EAS versus 59.1 W m^{-2} per AAOD for NAE (figure 3 and table 4). More generally, of our four regions (including GLO), NAE yields the largest forcing efficiency. Qualitatively similar statements exist if we normalize by AA emissions (table 4). As discussed above, this could be related to several factors (including the location), but some of the enhanced NAE forcing efficiency is related to the type of aerosol species being reduced. NAE features a relatively large decrease in SO_4 which constitutes 73% of the total AAOD decrease. In contrast, a relatively small decrease in BC occurs at 7% of the AAOD decrease. This NAE aerosol species mixture (i.e. the part of the AAOD that is caused by SO_4, OA or BC) contributes to its positive ERF_{ari}, where positive non-cloud scattering dominates over negative non-cloud absorption. NAE ERF_{aci} is also relatively large and positive (second largest behind EAS), which may be related to the dominant cloud regime in the upper mid-latitudes (i.e. preponderance of low-level liquid clouds). We also note that NAE emission reductions started occurring in the late 1970s/early 1980s, and the region is less polluted than the others. This may increase the susceptibility of the cloud droplet number concentration to the CCN concentration, and enhance aerosol cloud interactions (Jia and Quaas 2023). In contrast to NAE, AFR has the weakest normalized ERF at 13.2 W m^{-2} per AAOD. This is again consistent with the relatively large contribution of BC to the total AAOD decrease for AFR, which drives its net negative ERF_{ari}.

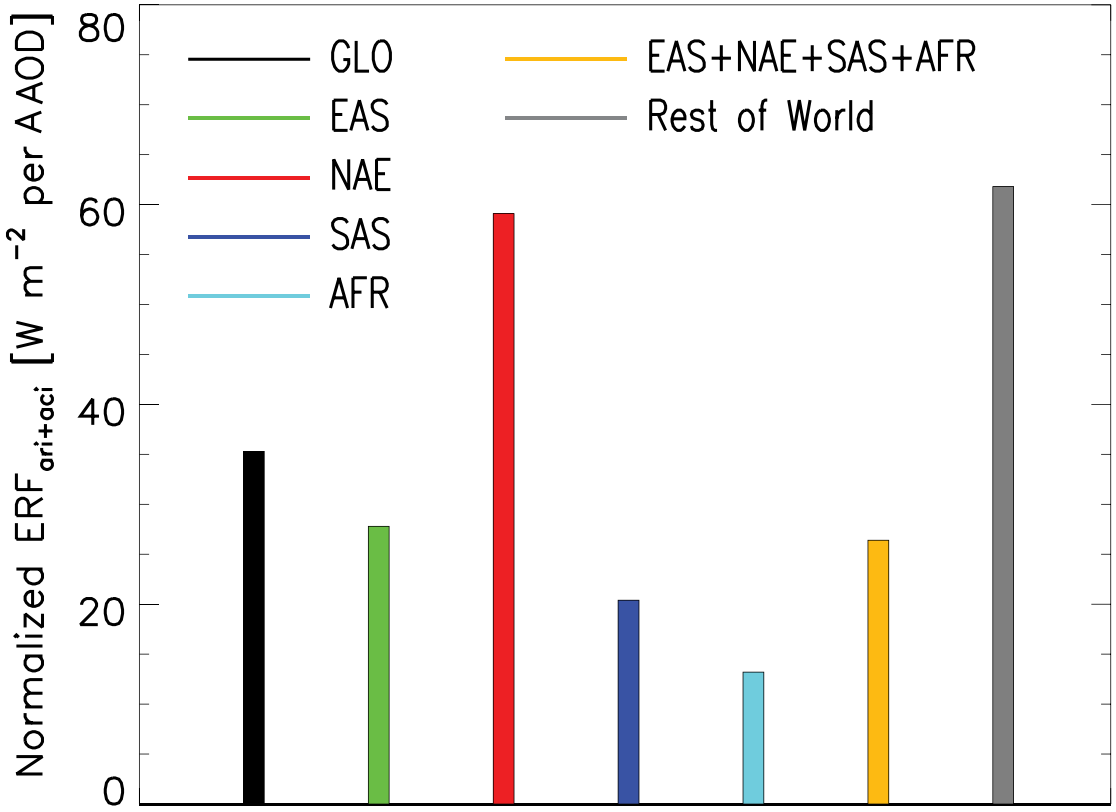

Figure 3. Global mean normalized ERF bar chart for the aerosol reduction signals. Bars show the global mean multimodel mean net ERF$_{ari+aci}$ normalized by the corresponding absolute value of the change in AAOD. Also included is the sum of the four regions (EAS + NAE + SAS + AFR) and its difference with GLO, i.e. the rest of the world. Units are W m^{-2} per AAOD.

3.8. ERF decomposition for the four regions and the rest of the world

We next compare the sum of the four regions (EAS + NAE + SAS + AFR) to GLO minus (EAS + NAE + SAS + AFR). Assuming linearity, the latter provides an estimate of the response to aerosol emissions reductions for the rest of the world, which includes South America, Central America, Australia, Russia and Indonesia. Our assumption of linearity may not be ideal, but RAMIP currently lacks actual rest of the world experiments (i.e. AA emissions reductions everywhere except our four regions). Future work, including actual rest of the world simulations with RAMIP models, will evaluate this assumption. The global mean AAOD decrease under EAS + NAE + SAS + AFR is -16.3 ± 2.4 10^{-3} (table 3), which constitutes the bulk (75%) of the corresponding decrease for GLO. The mixture of the aerosol species decrease under EAS + NAE + SAS + AFR is essentially identical (±1%) to that under GLO at 53% for SO_4 AOD, 33% for OA AOD and 14% for BC AOD. In contrast, the rest of the world accounts for only 25% of the AAOD decrease under GLO, and the mixture of the aerosol species decrease is less absorbing (53% for SO_4 AOD, 38% for OA AOD and 9% for BC AOD). Similar statements exist based on emissions, where the rest of the world accounts for only 27% of the AA emissions decrease under GLO.

Figure 4 shows the global mean ERF decomposition based on the global aerosol reduction signal (as in figure 2), along with that from the sum of the four regional perturbations, and the corresponding difference, i.e. the rest of the world. The sum of the four regions yields a significant increase in net ERF$_{ari+aci}$ at 0.43 ± 0.22 W m^{-2} (see also supplementary table 2), which corresponds to 56% of the increase in net ERF$_{ari+aci}$ under global aerosol reductions. As EAS + NAE + SAS + AFR captures a higher percentage (75%) of the GLO decrease in AAOD, 56% is below what one (naively) expects assuming a linear relationship between ERF and AAOD (and emissions). Stated in other words, the AAOD decrease for the rest of the world comprises only 25% of the GLO decrease, but 44% of the net ERF$_{ari+aci}$ increase. This forcing efficiency difference is also apparent in the normalized (by AAOD) net ERF$_{ari+aci}$, which is 26.4 W m^{-2} per AAOD for the sum of the four regions relative to 61.8 W m^{-2} per AAOD for the rest of the world (figure 3). Qualitatively similar statements exist if we normalize by AA emissions (supplementary table 2). Here, normalized (by AA emissions) net ERF$_{ari+aci}$ is 0.0059 W m^{-2}

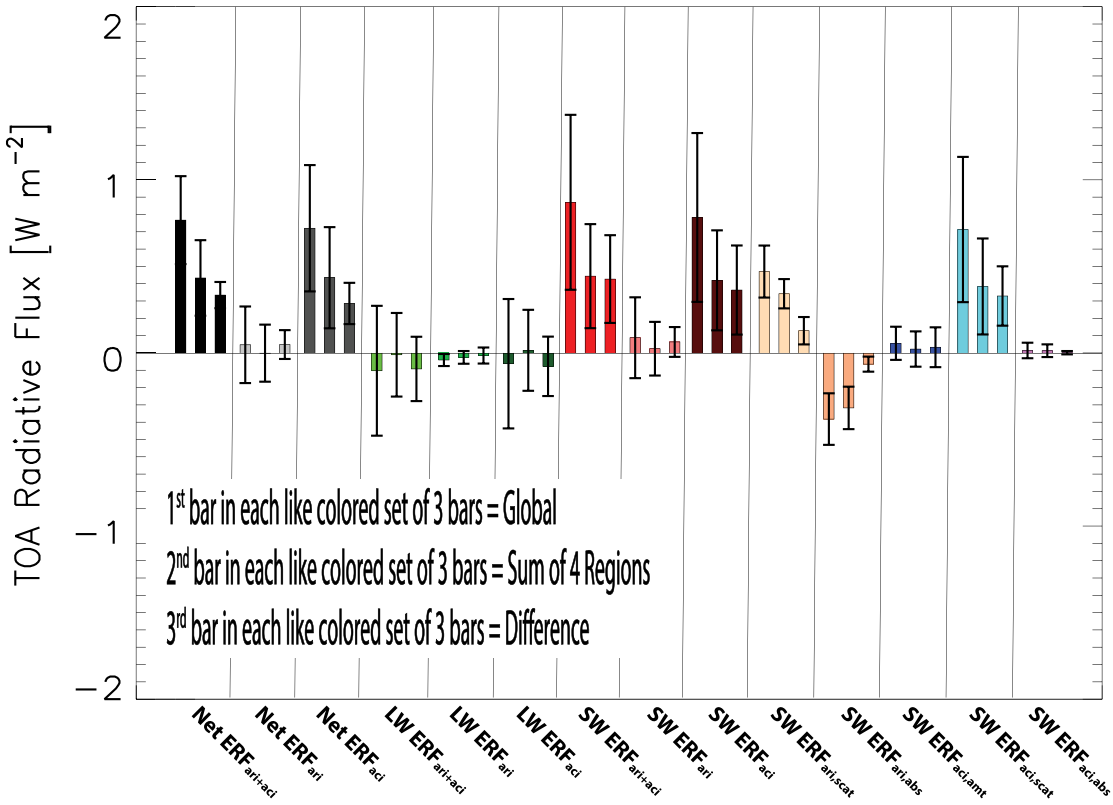

Figure 4. Global mean ERF decomposition bar chart for the global aerosol reduction signal, including the sum of the four regions and the corresponding difference. Bars show the global mean multimodel mean ERF decomposition, with the corresponding error bars representing the intermodal spread (±1 standard deviations across the models). The first bar in each like-colored set of 3 bars shows the global aerosol reduction signal. The second bar in each like-colored set of 3 bars shows the sum of the four regions (EAS + NAE + SAS + AFR). The third bar in each like-colored set of 3 bars shows the rest of the world (i.e. GLO minus EAS + NAE + SAS + AFR). To preserve figure clarity, individual model results are not included. Units are W m^{-2}.

per Tg year^{-1} for the sum of the four regions relative to 0.0123 W m^{-2} per Tg year^{-1} for the rest of the world.

The relatively weak increase (compared to the decrease in AAOD) in EAS + NAE + SAS + AFR net ERF$_{ari+aci}$ is related to SW radiative effects, as SW ERF$_{ari+aci}$ is 0.44 ± 0.30 W m^{-2} which is nearly identical to the corresponding increase for the rest of the world at 0.43 ± 0.25 W m^{-2} (figure 4 and supplementary table 2). This, in turn, is related to both aerosol-cloud and aerosol-radiation interactions. SW ERF$_{aci}$ is 0.42 ± 0.29 W m^{-2} for the sum of the four regions versus 0.36 ± 0.26 W m^{-2} outside of these four regions. Most of this is associated with the cloud scattering term at 0.38 ± 0.28 W m^{-2} and 0.33 ± 0.17 W m^{-2}, respectively. These SW ERF$_{aci,scat}$ values represent 54% and 46% of the corresponding GLO values (which are very similar to the corresponding percentages discussed above based on net ERF$_{ari+aci}$). These percentages are again below what one expects assuming linearity. We suggest this is in part related to the non-linearity of aerosol-cloud interactions, which become saturated in more polluted regions with higher background aerosol (e.g. Jia and Quaas 2023). Our four target regions were chosen because they are among the largest AA emitters (in particular EAS and SAS) and thus comprise relatively polluted environments. In contrast, the areas outside of these four regions are not among the largest AA emitters and therefore comprise a less polluted environment. For the same unit reduction in aerosol emissions for both regions, larger aerosol-cloud interactions would be expected in the cleaner environment. Furthermore, some of the emissions reductions outside our four main regions (e.g. South America) occur in close proximity to marine stratocumulus cloud decks, which likely leads to a large contribution through aerosol-cloud interactions.

Aerosol-radiation interactions (although not significant overall) also contribute to the relatively weak increase in EAS + NAE + SAS + AFR net ERF$_{ari+aci}$, and this is related to the type of aerosol species being reduced. As mentioned above, the mixture of the AAOD decrease under EAS + NAE + SAS + AFR contains a higher proportion of absorbing as opposed to scattering aerosols

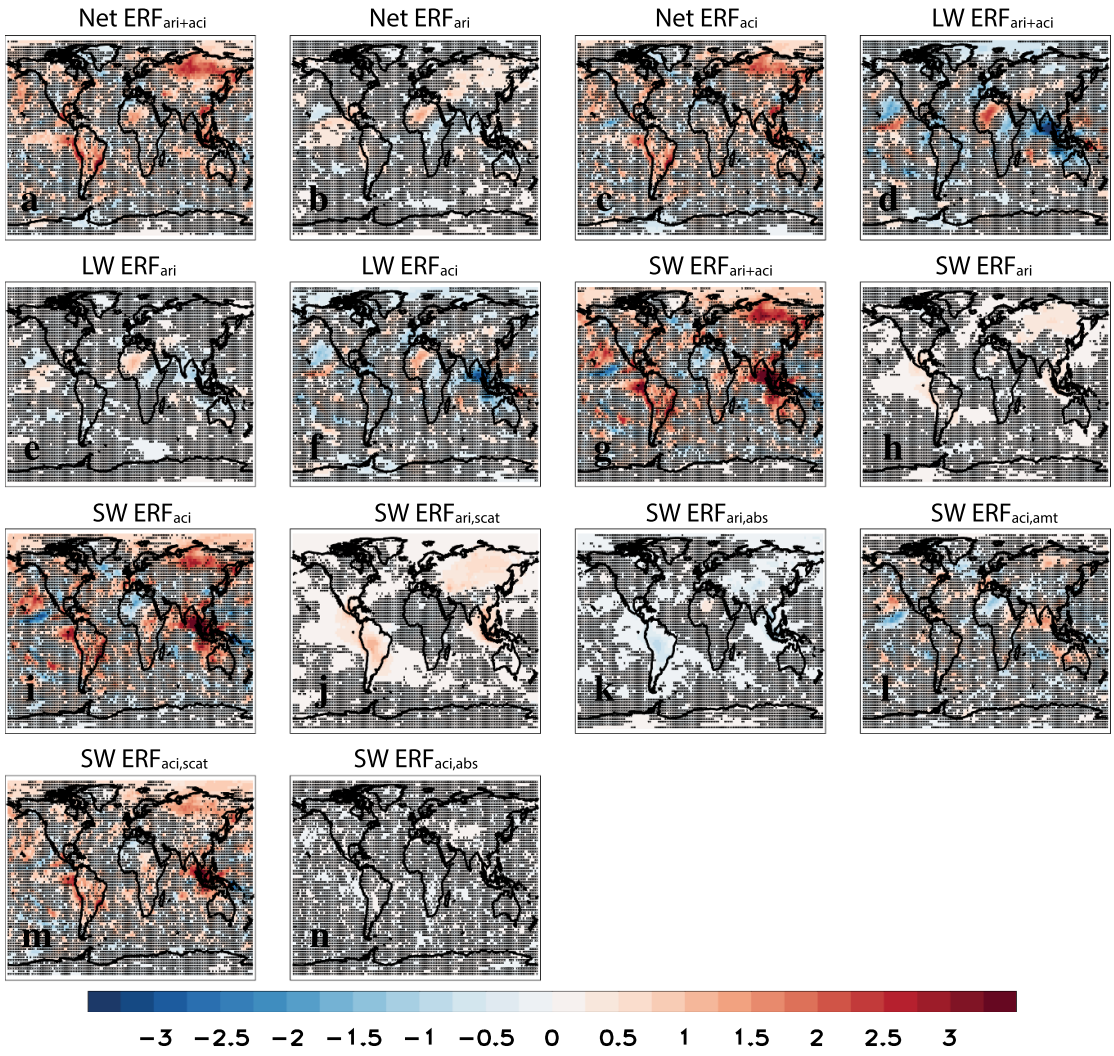

Figure 5. Spatial maps of the multimodel mean ERF decomposition for the global aerosol reduction signal minus the sum of the 4 regions (EAS + NAE + SAS + AFR). Non-stippled regions indicate grid boxes where at least 7 out of the 9 models agree on the sign. Units are W m^{-2}.

as compared to the rest of the world. This will promote cooling via reduced non-cloud absorption, muting the warming from reduced non-cloud scattering associated with SO_4 reductions. This is supported by SW ERF$_{ari}$, which is less positive at 0.02 ± 0.16 W m^{-2} under EAS + NAE + SAS + AFR as compared to 0.07 ± 0.09 W m^{-2} outside of these regions (figure 4 and supplementary table 2). The corresponding non-cloud scattering and non-cloud absorbing terms are 0.34 ± 0.09 W m^{-2} and −0.32 ± 0.12 W m^{-2} for EAS + NAE + SAS + AFR versus 0.13 ± 0.08 W m^{-2} and −0.06 ± 0.04 W m^{-2} for the rest of the world. Thus, although the sum over the four regions yields larger magnitude terms, non-cloud scattering and non-cloud absorption are nearly equal but opposite in magnitude and effectively cancel out. In contrast, for the rest of the world (where BC AOD reductions are only 9% of the total AAOD decrease), non-cloud scattering dominates over non-cloud absorption, driving a net increase in SW ERF$_{ari}$.

Figure 5 shows spatial maps of the ERF decomposition based on GLO minus our four regions, i.e. the effects of AA reductions for the rest of the world. The bulk of the net ERF$_{ari+aci}$ increase occurs over South America (extending over the eastern Pacific), central/eastern northern Russia and Indonesia (figure 5(a)). Although net ERF$_{ari}$ contributes (largely over Russia and the eastern Pacific; figure 5(b)), most of the signal is due to net ERF$_{aci}$ (figure 5(c)). These signals are particularly prominent in the SW (figures 5(g)–(i)) and to some extent muted in the LW, particularly over Indonesia (figures 5(d)–(f)). Figures 5(j) and (k) shows the importance of non-cloud scattering dominating over non-cloud absorption; the dominant term, however, remains SW ERF$_{aci,scat}$ (figure 5(m)). Thus, most of the increase in net ERF$_{ari+aci}$ for the rest of the world originates from South America, Russia and Indonesia.

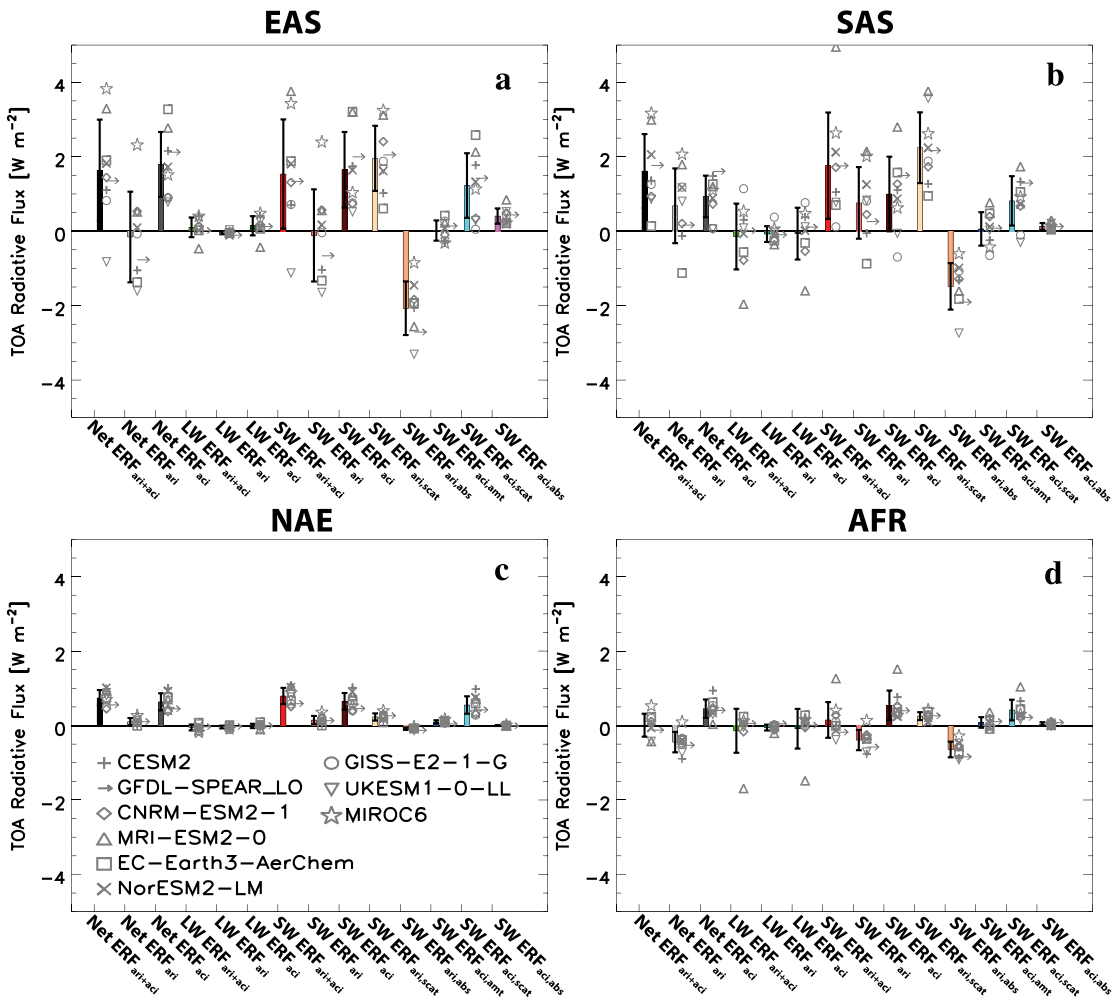

Figure 6. The impact of regional aerosol reductions on that region. Regional mean ERF decomposition bar chart for the (a) EAS; (b) SAS); (c) NAE; and (d) AFR aerosol reduction signals. Bars show the regional mean (over the same region as the aerosol reduction) multimodel mean ERF decomposition, with the corresponding error bars representing the intermodal spread (±1 standard deviations across the models). Gray symbols show individual model results. Units are W m^{-2}. Note that the *y*-axis spans −4–4 W m^{-2} in all panels.

3.9. Regional ERF decomposition

Although our focus has been on the global mean ERF, aerosols are heterogeneous and short-lived and thus will have larger impacts closer to their emission sources. Figure 6 shows bar charts of the ERF decomposition based on regional mean ERFs (over that region) for each of our four regional aerosol reduction signals. The regional mean EAS ERF is calculated over the EAS region; the regional mean SAS ERF is calculated over the SAS region, etc. Except for AFR, the regional mean net $ERF_{ari+aci}$ is larger than the corresponding global mean net $ERF_{ari+aci}$. EAS yields a regional mean net $ERF_{ari+aci}$ of 1.64 ± 1.36 W m^{-2} (figure 6(a) and supplementary table 3) followed closely by SAS at 1.61 ± 1.00 W m^{-2} (figure 6(b)). NAE yields a corresponding value of 0.74 ± 0.21 W m^{-2} (figure 6(c)) and AFR continues to yield a non-significant value of 0.01 ± 0.31 W m^{-2} (figure 6(d)).

As with the global mean ERF analysis, similar overall conclusions exist including the importance of aerosol-cloud interactions (net ERF_{aci} dominates the regional net $ERF_{ari+aci}$ for all four regions), with reduced SW cloud scattering the dominant term. However, larger intermodal spread occurs for the regional mean ERFs. This is particularly the case for EAS, where the intermodel net $ERF_{ari+aci}$ spread is −0.82 W m^{-2} in UKESM1-0-LL to 3.83 W m^{-2} in MIROC6 (figure 6(a)). SAS also features relatively large intermodal spread (figure 6(b)). Nonetheless, we emphasize that these relatively large multimodel mean regional ERFs will in turn drive relatively large regional climate impacts, which continue to be underappreciated in most policy discussions.

We also briefly evaluate the impact of regional versus global aerosol reductions on that region's net $ERF_{ari+aci}$ (figure 7). The corresponding difference (global minus regional) yields the impact of remote aerosol emission reductions on that region's net $ERF_{ari+aci}$. For each of our four regions, global aerosol

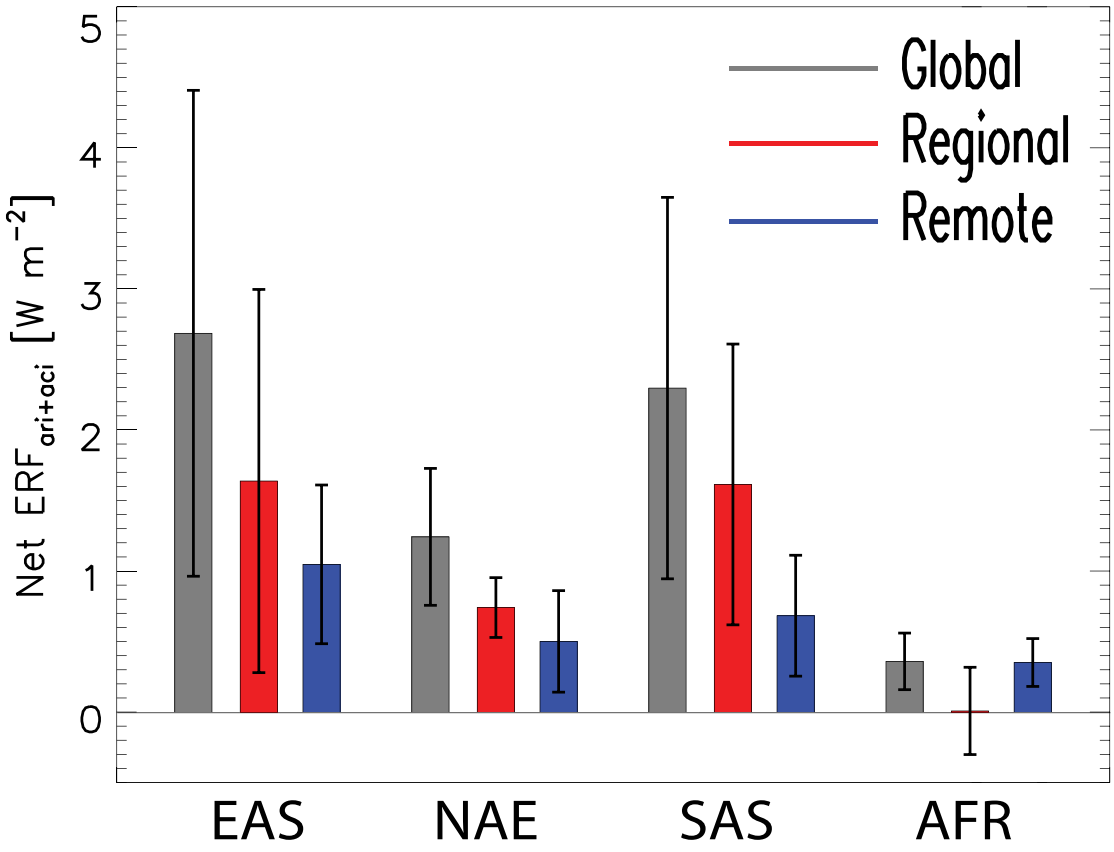

Figure 7. The impact of remote aerosol reductions on each region. Bars show the regional mean multimodel mean net $ERF_{ari+aci}$ based on the global aerosol reduction signal (gray) and that region's aerosol reduction signal (red) for our four regions (*x*-axis). The difference (global minus regional) yields the regional mean multimodel mean net $ERF_{ari+aci}$ associated with remote aerosol emission reductions. Error bars represent the intermodal spread (±1 standard deviations across the models). Units are W m^{-2}.

reductions drive a larger increase in that region's net $ERF_{ari+aci}$ as compared to regional aerosol emission reductions from that region. Illustrating with EAS, global aerosol emission reductions yield a net $ERF_{ari+aci}$ over the EAS region of 2.69 ± 1.72 W m^{-2}, which can be compared to the above discussed value of 1.64 ± 1.36 W m^{-2} for EAS aerosol emission reductions alone. This implies the impact of remote (outside of the EAS region) aerosol emission reductions yields a net $ERF_{ari+aci}$ over the EAS region of 1.05 ± 0.56 W m^{-2}. As a percentage, 61% of the net $ERF_{ari+aci}$ over the EAS region from global aerosol emission reductions is due to local aerosol emission reductions from that region (i.e. EAS) and 39% is due to remote (i.e. outside of the EAS region) aerosol emission reductions. This result clearly shows that remote emission reductions represent a sizable contribution (via transport). This statement is true for the other regions as well. For the NAE region, the breakdown is 60% from regional aerosol emission reductions and 40% from remote reductions. For the SAS region, the breakdown is 70% from regional reductions and 30% from remote reductions. Remote emission reductions (although smaller in magnitude at 0.35 ± 0.17 W m^{-2}) are most important for the AFR region at 97% versus 3% for regional aerosol emission reductions. The implication of these findings is that remote aerosol emission reductions have the capacity to significantly increase other countries' net $ERF_{ari+aci}$, which in turn will drive warming and associated climate impacts for the other countries. Furthermore, regional aerosol emission reductions can generate climate anomalies downstream of the emissions region via teleconnections (e.g. Undorf *et al* 2018, Wilcox *et al* 2019, Amiri-Farahani *et al* 2020).

3.10. Global mean seasonal ERFs

We briefly present global mean multimodel mean seasonal mean ERFs (supplementary table 4 and supplementary figure 16) for December–January–February (DJF); March-April-May (MAM); June–July–August (JJA); and September–October–November. Except for AFR during DJF and MAM, all seasonal multimodel mean ERFs are significant. Outside of SAS, which has minimal seasonal ERF variation, the maximum seasonal mean ERF occurs in JJA while the minimum occurs in DJF. Under GLO, for example, the JJA and DJF ERFs are 0.97 ± 0.22 W m^{-2} and 0.56 ± 0.12 W m^{-2}, respectively. The JJA forcing is 73% larger than the DJF forcing for GLO and EAS; for NAE, it is 120% larger. Seasonal

ERF variations are largely due to seasonal variations in emissions and climate. However, relatively small seasonal variation exists in our AA perturbations, which also show maximum AA reductions in DJF as opposed to JJA (opposite the seasonal ERF signal). For example, GLO yields DJF SO_2 decreases of -18.9 Tg versus JJA SO_2 decreases of -17.5 Tg. Thus, the seasonal ERF variations found here are largely due to climate. Although many climate-related factors likely contribute, our results are in general consistent with seasonal changes in sunlight. As most of the AA reductions occur in the NH for the majority of our perturbations (e.g. GLO, EAS and NAE), maximum sunlight occurs during summertime JJA and minimum sunlight occurs during wintertime DJF, consistent with the seasonal cycle of ERF for these regions. This argument is also consistent with the lack of seasonal ERF variations for SAS, as it is at a lower-latitude location (5–35 N) with less seasonal sunlight variation. Interestingly, there does not appear to be a strong monsoonal imprint on the SAS seasonal ERFs, i.e. the monsoon tends to peak during summertime (and the associated precipitation and wet removal) yet the JJA ERF remains relatively large. The importance of available sunlight to seasonal ERF variations is also clear by comparing the DJF versus JJA ERF maps under GLO (supplementary figure 16). Minimal positive DJF ERF occurs poleward of about 50 N (consistent with limited sunlight) whereas relatively large positive JJA ERF occurs at these higher NH latitudes (consistent with abundant sunlight).

4. Discussion and conclusions

RAMIP is designed to quantify the forcing and climate impacts of mid-21st century (year 2050) AA and precursor gas emissions reductions, by comparing an SSP3-7.0 (weak levels of air quality control) to an SSP1-2.6 (strong levels of air quality control) aerosol emission pathway. In all cases, 'AA and precursor gas emissions' includes both industrial and biomass burning emissions of sulfur dioxide, sulfate, BC, and OA. However, the bulk of the emissions decrease is due to industrial (as opposed to biomass burning) emissions. For GLO, for example, 99% of the decrease in SO_2 emissions is due to industrial emissions. The corresponding percentages for OA and BC are 84% and 97%, respectively.

Using five RAMIP experiments, we have quantified and decomposed the aerosol ERF, including aerosol radiation interactions and aerosol cloud interactions. The multi-model mean global mean net $ERF_{ari+aci}$ is 0.77 ± 0.25 W m^{-2} for GLO, which represents more than 70% of the magnitude of the historical (2015 relative to 1850) net $ERF_{ari+aci}$. Three of the four regional perturbations yield a significant positive net $ERF_{ari+aci}$ at 0.15 ± 0.07 W m^{-2} for EAS, 0.13 ± 0.09 W m^{-2} for NAE and 0.10 ± 0.05 W m^{-2} for SAS. AFR yields a positive but nonsignificant value at 0.05 ± 0.07 W m^{-2}. In all cases, net $ERF_{ari+aci}$ is dominated by aerosol-cloud interactions, which in turn are largely due to reduced cloud scattering. Aerosol-radiation interactions are smaller in magnitude, due to cancellation between positive non-cloud scattering and negative non-cloud absorption terms. Although the global net $ERF_{ari+aci}$ for the four regional perturbations are relatively small, the heterogeneous nature of aerosols implies that their impacts on climate could be large.

Of the four regional aerosol reduction signals, NAE yields the largest forcing efficiency at 59.1 W m^{-2} per AAOD whereas AFR yields the weakest at 13.2 W m^{-2} per AAOD. These differences are in part related to the type of aerosol species being reduced. NAE features a relatively large decrease in SO_4 (the primary scattering species that also acts as an efficient CCN) which constitutes 73% of the AAOD decrease, but a relatively small decrease in BC (the primary absorbing species) at 7% of the total AAOD decrease. In contrast, AFR features a relatively large contribution from BC (21%) to the total AAOD decrease, but a relatively small contribution from SO_4 at 36% of the total AAOD decrease. Analogous statements exist based on emissions (as opposed to AAOD).

We have shown the ERF responses exhibit spatial nonlinearities, which is related to the type of aerosol species being reduced, as well as to how polluted the background climate is, i.e. saturation of aerosol-cloud interactions are expected under more polluted backgrounds. Proximity to marine stratocumulus cloud decks also appears to be important (e.g. South America). Although the areas outside our four target regions (i.e. rest of the world) contribute 25% to the GLO AAOD reduction (27% based on AA emissions), they disproportionately contribute 44% to the GLO net $ERF_{ari+aci}$. This implies that the climate impacts of future aerosol reductions from polluted versus non-polluted regions may be of comparable magnitude, even if the latter involves smaller aerosol reductions. We caution, however, that our rest of the world signal assumes linearity, as it is based on the difference between GLO and (EAS + NAE + SAS + AFR). Future RAMIP plans will perform actual rest of the world simulations (i.e. AA emissions reductions for everywhere except our four regions) with a subset of the models, which will allow us to assess our current assumption of linearity. This finding also motivates augmentation of our RAMIP protocol to include regional aerosol emission experiments in some of these less polluted

regions, in particular South America, Russia and Indonesia. Alternatively, this is perhaps best explored in RAMIP version 2.0.

We have also shown that the multimodel regional mean net $ERF_{ari+aci}$ for three of the four regional perturbations is much larger (up to 1.64 ± 1.36 W m^{-2} for EAS) than the corresponding global mean value. However, these regional values are even larger (up to 2.69 ± 1.72 W m^{-2} for EAS) under global aerosol reductions, implying remote emission reductions represent a sizable contribution (up to 1.05 ± 0.56 W m^{-2} for EAS). The implication of these findings is that remote aerosol emission reductions have the capacity to significantly increase other countries' net $ERF_{ari+aci}$.

Although this analysis focuses on fixed SST experiments and the ERF, ongoing RAMIP analyses will quantify the full suite of climate responses to plausible near-term regional aerosol emissions reductions (using 10 ensemble member coupled ocean-atmosphere simulations). Based on the present study, we find that remote aerosol emission reductions have the capacity to significantly increase other countries' net $ERF_{ari+aci}$. RAMIP coupled simulations could be used to determine if these remote emission reductions will drive warming and associated climate impacts for the other countries. RAMIP coupled simulations could also be used to explore the extent to which such remote aerosol emission reductions impact the air quality of the other countries. If substantial, the implication is that a given country may not be able to reduce air pollution to a desired level though local aerosol emission reductions alone. Such findings could help inform international climate agreements and regional air quality frameworks.

Acknowledgment

We acknowledge support by the Center for Advanced Study in Oslo, Norway which funded and hosted the HETCLIF centre during the academic year of 2023/24. The NorESM simulations were enabled by resources provided by the National Academic Infrastructure for Supercomputing in Sweden (NAISS). We also acknowledge the following funding sources: Research Council of Norway Grant 324182 (CATHY; BHS, LJW, RJA, AMLE). Horizon Europe Grant 101137639 (CleanCloud; BHS, LJW, AMLE). National Science Foundation Grant AGS-2153486 (RJA). Natural Environment Research Council (NERC) Grant TerraFIRMA NE/W004895/1 (LJW, PTG, STR). National Center for Atmospheric Science, UK (LJW, STR, SA). Environment Research and Technology Development Fund (JPMEERF20232001) of the Environmental Restoration and Conservation Agency provided by Ministry of the Environment of Japan (TK, NO). Arctic Challenge for Sustainability 3 (ArCS-3), Program Grant Number JPMXD1720251001 (TK, NO). Global Environmental Research Coordination System from the Ministry of the Environment of Japan Grant MLIT2253 (TK, NO). H2020 Societal Challenges Grant No. 101003826 (JM, RM, DOD). Research Council Finland Grant No. 337552. (JM, RM, DOD). Columbia Center for Climate and Life (DMW). Natural Sciences and Engineering Research Council of Canada (NSERC) (PK, LJF). Swedish Research Council through Grant Agreements No. 2022-06725 (AL, AMLE) and 2020–04158 (AMLE). The U.S. National Oceanic and Atmospheric Administration under award NA23OAR4310601 (GP). Environment Research and Technology Development Fund (JPMEERF21S12010) of the Environmental Restoration and Conservation Agency provided by Ministry of the Environment of Japan (TT). This work was also supported by the University of Reading Advancing the Frontiers of Earth System Prediction (AFESP) Programme [award number A3720200] (SA). Climate modeling at GISS is supported by the NASA Modeling, Analysis and Prediction program, and resources supporting this work were provided by the NASA High-End Computing (HEC) Program through the NASA Center for Climate Simulation (NCCS) at Goddard Space Flight Center.

Data availability statement

The data that support the findings of this study will be openly available after acceptance (but before publication) at the following URL/DOI: https://esgf.github.io/nodes.html.

Supplementary data 1 available at https://doi.org/10.1088/2752-5295/ae5418/data1.

Conflict of interest

The authors declare that the research was conducted in the absence of any commercial or financial relationships that could be construed as a potential conflict of interest.

Code availability statement

The Python-based radiative kernel toolkit and the GFDL radiative kernel can be downloaded from https://climate.rsmas.miami.edu/data/radiative-kernels/. The APRP code can be downloaded from https://zenodo.org/records/8206763.

ORCID iDs

Robert J Allen 0000-0003-1616-9719
Bjørn H Samset 0000-0001-8013-1833
Sharar Ahmadi 0000-0002-2754-4820
Annica M L Ekman 0000-0002-5940-2114
Maxwell T Elling 0000-0001-6091-809X
Luke Fraser-Leach 0009-0003-9452-5528
Paul Griffiths 0000-0002-1089-340X
James Keeble 0000-0003-2714-1084
Paul Kushner 0000-0002-6404-4518
Anna Lewinschal 0009-0000-9526-4524
Risto Makkonen 0000-0002-8961-3393
Joonas Merikanto 0000-0002-1145-2569
Pierre Nabat 0000-0001-7034-638X
Declan O'Donnell 0000-0002-2700-471X
Naga Oshima 0000-0002-8451-2411
Geeta Persad 0000-0003-4690-0867
Toshihiko Takemura 0000-0002-2859-6067
Kostas Tsigaridis 0000-0001-5328-819X
Knut von Salzen 0000-0002-2991-6181
Daniel M Westervelt 0000-0003-0806-9961

References

Aas W *et al* 2019 Global and regional trends of atmospheric sulfur *Sci. Rep.* **9** 953
Acosta Navarro J C *et al* 2017 Future response of temperature and precipitation to reduced aerosol emission as compared with increased greenhouse gas concentrations *J. Clim.* **30** 939–54
Albrecht B A 1989 Aerosols, cloud microphysics, and fractional cloudiness *Science* **245** 1227–30
Allen R J *et al* 2020 Climate and air quality impacts due to mitigation of non-methane near-term climate forcers *Atmos. Chem. Phys.* **20** 9641–63
Allen R J 2025 *piClim-370 Data Produced by the CESM2 Model for the Regional Aerosol Model Intercomparison Project (RAMIP)* (NERC EDS Centre for Environmental Data Analysis) (https://doi.org/10.5285/fc7d9281c75b4acd99ad23f5f36ee7fc)
Allen R J, Amiri-Farahani A, Lamarque J F, Smith C, Shindell D, Hassan T and Chung C E 2019 Observationally constrained aerosol–cloud semi-direct effects *npj Clim. Atmos. Sci.* **2** 16
Allen R J, Samset B H, Wilcox L J and Fisher R A 2024 Are Northern Hemisphere boreal forest fires more sensitive to future aerosol mitigation than to greenhouse gas–driven warming? *Sci. Adv.* **10** eadl4007
Allen R J and Sherwood S C 2010 Aerosol-cloud semi-direct effect and land-sea temperature contrast in a GCM *Geophys. Res. Lett.* **37** L07702
Amiri-Farahani A, Allen R J, Li K-F, Nabat P and Westervelt D M 2020 A La Niña-like climate response to south African biomass burning aerosol in CESM simulations *J. Geophys. Res.: Atmos.* **125** e2019JD031832
Bellouin N *et al* 2020 Bounding global aerosol radiative forcing of climate change *Rev. Geophys.* **58** e2019RG000660
Benas N, Meirink J F, Roebeling R and Stengel M 2025 Analysis of ship emission effects on clouds over the southeastern Atlantic using geostationary satellite observations *Atmos. Chem. Phys.* **25** 6957–73
Boucher O *et al* 2013 Clouds and aerosols *Climate Change 2013: The Physical Science Basis. Working Group I Contribution to the Fifth Assessment Report of the Intergovernmental Panel on Climate Change* ed T F Stocker *et al* (Cambridge University Press) pp 571–658
Danabasoglu G *et al* 2020 The community earth system model version 2 (CESM2) *J. Adv. Model. Earth Syst.* **12** e2019MS001916
Delworth T L *et al* 2020 SPEAR: the next generation GFDL modeling system for seasonal to multidecadal prediction and projection *J. Adv. Model. Earth Syst.* **12** e2019MS001895
Diamond M S 2023 Detection of large-scale cloud microphysical changes within a major shipping corridor after implementation of the International Maritime Organization 2020 fuel sulfur regulations *Atmos. Chem. Phys.* **23** 8259–69
Eyring V, Bony S, Meehl G A, Senior C A, Stevens B, Stouffer R J and Taylor K E 2016 Overview of the coupled model intercomparison project phase 6 (CMIP6) experimental design and organization *Geosci. Model. Dev.* **9** 1937–58
Forster P M, Richardson T, Maycock A C, Smith C J, Samset B H, Myhre G, Andrews T, Pincus R and Schulz M 2016 Recommendations for diagnosing effective radiative forcing from climate models for CMIP6 *J. Geophys. Res.: Atmos.* **121** 12,460–75
Forster P *et al* 2021 The Earth's energy budget, climate feedbacks, and climate sensitivity *Climate Change 2021: The Physical Science Basis. Contribution of Working Group I to the Sixth Assessment Report of the Intergovernmental Panel on Climate Change* ed V Masson-Delmotte *et al* (Cambridge University Press) pp 923–1054

Gettelman A, Christensen M W, Diamond M S, Gryspeerdt E, Manshausen P, Stier P, Watson-Parris D, Yang M, Yoshioka M and Yuan T 2024 Has reducing ship emissions brought forward global warming? *Geophys. Res. Lett.* **51** e2024GL109077
Ghan S J 2013 Technical note: estimating aerosol effects on cloud radiative forcing *Atmos. Chem. Phys.* **13** 9971–4
Griffiths P T *et al* 2025 Opinion: the role of AerChemMIP in advancing climate and air quality research *Atmos. Chem. Phys.* **25** 8289–328
Gryspeerdt E *et al* 2017 Constraining the instantaneous aerosol influence on cloud albedo *Proc. Natl Acad. Sci. USA* **114** 4899–904
Hodnebrog Ø *et al* 2024 Recent reductions in aerosol emissions have increased Earth's energy imbalance *Commun. Earth Environ.* **5** 166
Hoesly R M *et al* 2018 Historical (1750–2014) anthropogenic emissions of reactive gases and aerosols from the Community Emissions Data System (CEDS) *Geosci. Model. Dev.* **11** 369–408
Iles C E, Samset B H, Sandstad M, Schuhen N, Wilcox L J and Lund M T 2024 Strong regional trends in extreme weather over the next two decades under high- and low-emissions pathways *Nat. Geosci.* **17** 845–50
Jia H and Quaas J 2023 Nonlinearity of the cloud response postpones climate penalty of mitigating air pollution in polluted regions *Nat. Clim. Change* **13** 943–50
Jordan G and Henry M 2024 IMO2020 regulations accelerate global warming by up to 3 years in UKESM1 *Earth's Future* **12** e2024EF005011
Kalisoras A *et al* 2024 Decomposing the effective radiative forcing of anthropogenic aerosols based on CMIP6 Earth system models *Atmos. Chem. Phys.* **24** 7837–72
Kelley M *et al* 2020 GISS-E21: configurations and climatology *J. Adv. Model. Earth Syst.* **12** e2019MS002025
Koch D and Del Genio A D 2010 Black carbon semi-direct effects on cloud cover: review and synthesis *Atmos. Chem. Phys.* **10** 7685–96
Lewinschal A 2025 *piClim-370 Data Produced by the NorESM2-LM Model for the Regional Aerosol Model Intercomparison Project (RAMIP)* (NERC EDS Centre for Environmental Data Analysis) (https://doi.org/10.5285/c73e478afb4745d6966025049e4de53a)
Liu L *et al* 2018 A PDRMIP multimodel study on the impacts of regional aerosol forcings on global and regional precipitation *J. Clim.* **31** 4429–47
Masson-Delmotte V *et al* ed 2021 IPCC, 2021: summary for Policymakers *Climate Change 2021: The Physical Science Basis. Contribution of Working Group I to the Sixth Assessment Report of the Intergovernmental Panel on Climate Change* (Cambridge University Press) (https://doi.org/10.1017/9781009157896.001)
McDuffie E E, Smith S J, O'Rourke P, Tibrewal K, Venkataraman C, Marais E A, Zheng B, Crippa M, Brauer M and Martin R V 2020 A global anthropogenic emission inventory of atmospheric pollutants from sector- and fuel-specific sources (1970–2017): an application of the Community Emissions Data System (CEDS) *Earth Syst. Sci. Data* **12** 3413–42
Myhre G *et al* 2017 PDRMIP: a precipitation driver and response model intercomparison project—Protocol and preliminary results *Bull. Am. Meteorol. Soc.* **98** 1185–98
Myhre G *et al* 2013 Anthropogenic and natural radiative forcing *Climate Change 2013—The Physical Science Basis*. Working Group I Contribution to the Fifth Assessment Report of the Intergovernmental Panel on Climate Change ed T F Stocker *et al* (Cambridge University Press) pp 659–740
Nabat P 2025 *piClim-370 Data Produced by the CNRM-ESM2-1 Model for the Regional Aerosol Model Intercomparison Project (RAMIP)* (NERC EDS Centre for Environmental Data Analysis) (https://doi.org/10.5285/2dc9d53fa44e41c1b25f06c3a1be2374)
O'Donnell D, Makkonen R and Merikanto J 2025 *piClim-370 Data Produced by the EC-Earth3-AerChem Model for the Regional Aerosol Model Intercomparison Project (RAMIP)* (NERC EDS Centre for Environmental Data Analysis)
Oshima N and Koshiro T 2025 *piClim-370 Data Produced by the MRI-ESM2-0 Model for the Regional Aerosol Model Intercomparison Project (RAMIP)* (NERC EDS Centre for Environmental Data Analysis) (https://doi.org/10.5285/0a4b3c3b2d1f4510ba3544c1a81ee645)
Oshima N, Yukimoto S, Deushi M, Koshiro T, Kawai H, Tanaka T Y and Yoshida K 2020 Global and arctic radiative forcing of anthropogenic gases and aerosols in MRI-ESM2.0 *Prog. Earth Planet. Sci.* **7** 38
Paynter D 2025 *piClim-370 Data Produced by the GFDL-SPEAR_LO Model for the Regional Aerosol Model Intercomparison Project (RAMIP)* (NERC EDS Centre for Environmental Data Analysis)
Persad G *et al* 2023 Rapidly evolving aerosol emissions are a dangerous omission from near-term climate risk assessments *Environ. Res.: Clim.* **2** 032001
Pincus R and Baker M B 1994 Effect of precipitation on the albedo susceptibility of clouds in the marine boundary layer *Nature* **372** 250–2
Pincus R, Forster P M and Stevens B 2016 The radiative forcing model intercomparison project (RFMIP): experimental protocol for CMIP6 *Geosci. Model. Dev.* **9** 3447–60
Quaas J *et al* 2020 Constraining the Twomey effect from satellite observations: issues and perspectives *Atmos. Chem. Phys.* **20** 15079–99
Quaas J *et al* 2022 Robust evidence for reversal of the trend in aerosol effective climate forcing *Atmos. Chem. Phys.* **22** 12221–39
Quaglia I and Visioni D 2024 Modeling 2020 regulatory changes in international shipping emissions helps explain anomalous 2023 warming *Earth Syst. Dyn.* **15** 1527–41
Rosenfeld D, Kokhanovsky A, Goren T, Gryspeerdt E, Hasekamp O, Jia H, Lopatin A, Quaas J, Pan Z and Sourdeval O 2023 Frontiers in satellite-based estimates of cloud-mediated aerosol forcing *Rev. Geophys.* **61** e2022RG000799
Rumbold S, Ahmadi S, Wilcox L, Keeble J, Griffiths P, Lister G and Predoi V 2025 *piClim-370 Data Produced by the UKESM1-0-LL Model for the Regional Aerosol Model Intercomparison Project (RAMIP)* (NERC EDS Centre for Environmental Data Analysis)
Samset B H *et al* 2025 East Asian aerosol cleanup has likely contributed to the recent acceleration in global warming *Commun. Earth Environ.* **6** 543
Samset B H, Lund M T, Bollasina M, Myhre G and Wilcox L 2019 Emerging Asian aerosol patterns *Nat. Geosci.* **12** 582–4
Samset B H, Wilcox L J and Allen R J 2024 Broader research efforts and assessments needed to uncover the complex climate effects of regional changes in aerosol emissions *PLoS Clim.* **3** e0000508
Séférian R *et al* 2019 Evaluation of CNRM Earth-System model, CNRM-ESM2-1: role of Earth system processes in present-day and future climate *J. Adv. Model. Earth Syst.* **11** 4182–227
Seland Ø *et al* 2020 Overview of the Norwegian earth system model (NorESM2) and key climate response of CMIP6 DECK, historical, and scenario simulations *Geosci. Model. Dev.* **13** 6165–200
Sellar A A *et al* 2019 UKESM1: description and evaluation of the U.K. earth system model *J. Adv. Model. Earth Syst.* **11** 4513–58
Skeie R B, Byrom R, Hodnebrog Ø, Jouan C and Myhre G 2024 Multi-model effective radiative forcing of the 2020 sulfur cap for shipping *Atmos. Chem. Phys.* **24** 13361–70
Smith C J *et al* 2018 Understanding rapid adjustments to diverse forcing agents *Geophys. Res. Lett.* **45** 12,023–31
Smith C J *et al* 2020 Effective radiative forcing and adjustments in CMIP6 models *Atmos. Chem. Phys.* **20** 9591–618

Soden B J, Held I M, Colman R, Shell K M, Kiehl J T and Shields C A 2008 Quantifying climate feedbacks using radiative kernels *J. Clim.* **21** 3504–20
Stjern C W *et al* 2017 Rapid adjustments cause weak surface temperature response to increased black carbon concentrations *J. Geophys. Res.: Atmos.* **122** 11,462–81
Szopa S *et al* 2021 Short-lived climate forcers *Climate Change 2021: The Physical Science Basis. Contribution of Working Group I to the Sixth Assessment Report of the Intergovernmental Panel on Climate Change* ed V Masson-Delmotte *et al* (Cambridge University Press) pp 817–922
Takemura T 2025 *piClim-370 Data Produced by the MIROC6 Model for the Regional Aerosol Model Intercomparison Project (RAMIP)* (NERC EDS Centre for Environmental Data Analysis)
Tatebe H *et al* 2019 Description and basic evaluation of simulated mean state, internal variability, and climate sensitivity in MIROC6 *Geosci. Model. Dev.* **12** 2727–65
Taylor K E, Crucifix M, Braconnot P, Hewitt C D, Doutriaux C, Broccoli A J, Mitchell J F B and Webb M J 2007 Estimating shortwave radiative forcing and response in climate models *J. Clim.* **20** 2530–43
Thornhill G D *et al* 2021 Effective radiative forcing from emissions of reactive gases and aerosols—a multi-model comparison *Atmos. Chem. Phys.* **21** 853–74
Twomey S 1974 Pollution and the planetary albedo *Atmos. Environ.* **8** 1251–6
Twomey S 1977 The influence of pollution on the shortwave albedo of clouds *J. Atmos. Sci.* **34** 1149–52
Undorf S, Polson D, Bollasina M A, Ming Y, Schurer A and Hegerl G C 2018 Detectable impact of local and remote anthropogenic aerosols on the 20th Century changes of west African and South Asian monsoon precipitation *J. Geophys. Res.: Atmos.* **123** 4871–89
van Noije T *et al* 2021 EC-Earth3-AerChem: a global climate model with interactive aerosols and atmospheric chemistry participating in CMIP6 *Geosci. Model. Dev.* **14** 5637–68
von Salzen K, Akingunola A, Cole J N S, Digby R A R, Doherty S J, Fraser-Leach L, Gryspeerdt E, Sigmond M and Wood R 2025 Reduced aerosol pollution diminished cloud reflectivity over the North Atlantic and Northeast Pacific *Nat. Commun.* **16** 9433
Watson-Parris D *et al* 2025 Surface temperature effects of recent reductions in shipping SO_2 emissions are within internal variability *Atmos. Chem. Phys.* **25** 4443–54
Watson-Parris D and Smith C J 2022 Large uncertainty in future warming due to aerosol forcing *Nat. Clim. Change* **12** 1111–3
Westervelt D M, Conley A J, Fiore A M, Lamarque J-F, Shindell D, Previdi M, Faluvegi G, Correa G and Horowitz L W 2017 Multimodel precipitation responses to removal of U.S. sulfur dioxide emissions *J. Geophys. Res.: Atmos.* **122** 5024–38
Westervelt D M, Horowitz L W, Naik V, Golaz J-C and Mauzerall D L 2015 Radiative forcing and climate response to projected 21st century aerosol decreases *Atmos. Chem. Phys.* **15** 12681–703
Westervelt D M, Tsigaridis K, Nazarenko L and Elling M 2025 *piClim-370 Data Produced by the GISS-E2-1-G Model for the Regional Aerosol Model Intercomparison Project (RAMIP)* (NERC EDS Centre for Environmental Data Analysis)
Wilcox L J *et al* 2020 Accelerated increases in global and Asian summer monsoon precipitation from future aerosol reductions *Atmos. Chem. Phys.* **20** 11955–77
Wilcox L J *et al* 2023 The regional aerosol model intercomparison project (RAMIP) *Geosci. Model. Dev.* **16** 4451–79
Wilcox L J, Dunstone N, Lewinschal A, Bollasina M, Ekman A M L and Highwood E J 2019 Mechanisms for a remote response to Asian anthropogenic aerosol in boreal winter *Atmos. Chem. Phys.* **19** 9081–95
Yoshioka M, Grosvenor D P, Booth B B B, Morice C P and Carslaw K S 2024 Warming effects of reduced sulfur emissions from shipping *Atmos. Chem. Phys.* **24** 13681–92
Yuan T *et al* 2024 Abrupt reduction in shipping emission as an inadvertent geoengineering termination shock produces substantial radiative warming *Commun. Earth Environ.* **5** 281
Yukimoto S *et al* 2019 The meteorological research institute earth system model version 2.0, MRI-ESM2.0: description and basic evaluation of the physical component *J. Meteorol. Soc. Jpn. II* **97** 931–965.1202
Zelinka M D, Andrews T, Forster P M and Taylor K E 2014 Quantifying components of aerosol-cloud-radiation interactions in climate models *J. Geophys. Res.: Atmos.* **119** 7599–615
Zelinka M D, Smith C J, Qin Y and Taylor K E 2023 Comparison of methods to estimate aerosol effective radiative forcings in climate models *Atmos. Chem. Phys.* **23** 8879–98
Zheng B *et al* 2018 Trends in China's anthropogenic emissions since 2010 as the consequence of clean air actions *Atmos. Chem. Phys.* **18** 14095–111